Dissertation Research Proposal:

Temperature and Frequency Dependent Deterministic Phonon Transport Prediction of Thermal Conductivity in Lithium Aluminate

Nicholas H. Whitman

Advisor: Dr. Todd S. Palmer

School of Nuclear Science and Engineering

Oregon State University

Contents

1 INTRODUCTION AND BACKGROUND **6**

1.1 Thermal conductivity and phonon transport 6

1.2 Lithium aluminate, tritium, and predictive science 6

1.3 Purpose and scope of this work 12

2 RESEARCH OBJECTIVES **14**

2.1 Grey phonon transport 14

2.2 Homogeneous temperature and frequency dependent phonon transport 15

2.3 Heterogeneous temperature and frequency-dependent phonon transport 15

2.4 Possible difficulties with research objectives 16

3 PROPOSED METHOD **18**

3.1 Grey phonon transport 18

3.1.1 Continuum phonon transport physics 18

3.1.2 Grey phonon transport approximation 22

3.1.3 Heat transfer relations 24

3.1.4 Self-adjoint angular flux formulation of the SRT-PRT . 26

3.1.5 Discrete ordinates (S_N) angular discretization 27

3.1.6 Finite element spatial discretization 28

3.1.7 Grey iterative solution methodology 30

3.2 Temperature and frequency dependent phonon transport . . . 33

3.2.1 Description of temperature and frequency dependent approach 33

3.2.2 Frequency and temperature dependent phonon transport in the linearized approach 34
3.2.3 Angular discretization and spectral mapping 36
3.2.4 Frequency and temperature dependent pseudo-scattering algorithm 39
3.3 Phonon transport with material heterogeneity, interfacial scattering 41
3.3.1 Order parameter method for moving interfacial scattering into the grey BTE 41
3.3.2 Order parameter method for moving interfacial scattering into the frequency, temperature dependent BTE . . 46

4 EXPECTED SCHEDULE 48
4.1 Gantt Chart 48

5 TEST PROBLEMS 49
5.1 Grey phonon transport 49
5.1.1 Method of manufactured solutions spatial convergence study 49
5.1.2 Temperature calculation in silicon and lithium aluminate 53
5.1.3 Grey thermal conductivity estimate in lithium aluminate 55
5.2 Temperature and frequency dependent phonon transport . . . 56
5.2.1 Perfect lithium aluminate 56
5.3 Order parameter grey and frequency, temperature dependent phonon transport 58

6 PRELIMINARY RESULTS 59
6.1 Grey phonon transport 59

6.1.1 Method of manufactured solutions spatial convergence study 59
6.1.2 Temperature calculation in silicon and lithium aluminate 60
6.1.3 Grey thermal conductivity estimate in lithium aluminate 61

7 CONCLUDING REMARKS 64

8 ACKNOWLEDGEMENTS 66

9 APPENDIX 71

9.1 Appendix A: 131-group $LiAlO_2$ properties 71
9.2 Journal Articles and Contributed Summary 74

List of Figures

1 TPBAR schematic. 9

2 Tritium release prediction and actual tritium release vs. expected full power days (EPFD). 11

3 Integrated modeling road map created by the TTP program [12]. 12

4 Molecular dynamics informed angular quadrature. 37

5 Mean free path vs. temperature for each angle-energy group. . 37

6 $\gamma_g(T)$ computed by taking quotient of two polynomial fits. . . 38

7 Order parameter informed from phase field modeling. 42

8 1D slab order parameter test problem. 45

9 1D slab order parameter test problem results. 45

10 Unrefined orthogonal, linear, and quadratic meshes used in the MMS study. 53

11 2D periodic mesh used in temperature profile calculations. . . 54

12 Homogeneous material with isothermal boundary test case. . . 57

13 Heterogeneous material with thermal gradient test case. 58

14 Method of manufactured solutions spatial convergence study. . 59

15 Dimensionless temperature distribution for 3Λ thickness. . . . 60

16 Grey thermal conductivity profiles in lithium aluminate. . . . 62

17 Deviation from kinetic theory, abs. % difference. 62

List of Tables

1 MFEM bilinear and linear forms. 31

2 Example quadrature, weighting, and Λ grouping in the frequency and temperature dependent approach. 39

3 Grey silicon phonon data. 54

4 Grey lithium aluminate phonon data. 55

List of Algorithms

1 Grey Phonon Transport Source Iteration 32

2 An iterative algorithm for solving frequency and temperature dependent deterministic phonon transport equation in the SAAF form 40

3 An iterative algorithm for solving frequency and temperature dependent deterministic phonon transport equation in the SAAF form with order parameter correction 47

1 INTRODUCTION AND BACKGROUND

1.1 Thermal conductivity and phonon transport

Prior knowledge of the thermal conductivity of a material is important for performing thermal performance predictions. The physical measurement of a given material's thermal conductivity may be prohibitively expensive and difficult, either due to the exotic nature of the material or the extreme nature of the environment. Therefore, methods which can predict thermal conductivity are highly valuable and less costly to predictive science efforts.

Molecular dynamics, a first principles method, serves as a method for predicting a material's thermal conductivity *a priori*. These simulations, however, are limited by both simulation size and by classical physics. In larger simulation domain sizes, Boltzmann phonon transport simulations may be more attractive to capture bulk thermal transport behavior, and may more readily couple to multi-physics simulations.

Phonon transport predictions of thermal conductivity have historically focused on thin films and dielectrics in semi-conductor applications [1, 2]. Recent research has also shown promise in using deterministic methods for simulating Boltzmann phonon transport to predict thermal conductivity in larger scale ceramic applications, such as uranium dioxide or uranium dioxide with xenon impurities for nuclear reactor fuels [3].

1.2 Lithium aluminate, tritium, and predictive science

Lithium aluminate ($LiAlO_2$) is a ceramic material of significant interest to the fusion community as it is currently one of the most attractive materials for use

in neutronic fusion reactors due in part due to its large temperature operating range [4, 5]. Tritium (^{3}H) is one of the most common nuclear fusion fuels, favoring higher fusion probabilities with other nuclei at relatively lower temperature ranges, and can be produced through neutron absorption reactions in ^{6}Li, and threshold absorption reactions ^{7}Li. Tritium is also an important asset required to fulfill the U.S. Department of Energy/National Nuclear Security Administration's (DOE/NNSA) missions and must be replenished due its 12.3 year half-life [6, 7].

Under neutron irradiation, lithium aluminate's micro-structure changes drastically partially due to the respective density change during the precipitation of lithium pentaluminate ($LiAl_5O_8$) as lithium is depleted. Other smaller scale effects are also prevalent. The drastic change in micro-structure during in-reactor irradiation greatly influences heat transport at the micro-scale, making time-dependent thermal performance prediction difficult.

Current research into this material aims to better understand long term effects of irradiation-induced thermal performance degradation [8]. The goal of our research is to predict thermal conductivity in lithium aluminate as a function of neutron irradiation using Boltzmann transport simulations of phonons informed from molecular dynamics simulations. The thermal conductivity predictions will then serve as inputs in phase field evolution simulations that, for example, solve Cahn-Hilliard (coupled species diffusion) equations. Previous work in a uranium-molybdenum binary metal system has used similar phase field modeling approaches that may be applied similarly to lithium aluminate [9].

Lithium aluminate ($LiAlO_2$, lithium aluminum oxide) specifically in the γ-$LiAlO_2$ phase, is a ceramic material which has been identified as a primary

candidate for the breeding blanket material in the previously mentioned neutronic fusion reactors [10]. γ-$LiAlO_2$ is also primary material currently used in the large scale production of tritium to satisfy DOE/NNSA missions. Through both applications, this material's un-irradiated performance has been thoroughly documented. The material's irradiated performance and evolution, however, is more uncertain.

Part of the DOE/NNSA's mission requires a constant replenishment of tritium. The method currently used to replace the stockpile's decaying tritium is to irradiate lithium aluminate with neutrons inside of a power producing nuclear reactor, producing tritium gas in the process. Lithium aluminate enriched in $^{6}_{3}$Li and in an annular form are stacked in what are referred to as a Tritium Producing Burnable Absorber Rods (TPBAR)s [11, 12]. TPBARs, as illustrated in Figure 1, act as partial or full replacements for burnable poison rods in these reactors, and offer the same functionality of the neutronic reactivity control. The presence of these TPBARs, however, requires slightly higher levels of fuel enrichment due to the slightly higher negative reactivity present.

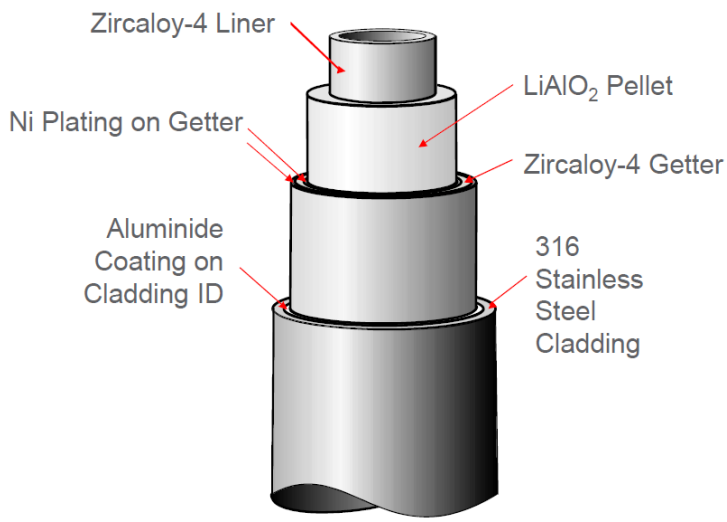

Figure 1: TPBAR schematic.

TPBARs are loaded into the reactor during refueling and stay there until they are removed after the current fuel cycle, which may last 16 to 24 months. During the course of neutron irradiation throughout the fuel cycle, the structure of the lithium aluminate changes drastically due to lithium burnup/depletion among other various mechanisms. As the fraction of lithium decreases, a secondary phase less rich in lithium becomes more thermodynamically favorable. This phase, lithium pentaluminate ($LiAl_5O_8$), is more dense than lithium aluminate. The increase in density causes voiding inside the local matrix where secondary phases precipitate.

Irradiation induced defects such as voids, dislocations, and point defects become prevelant in lithium aluminate as well as the lithium pentaluminate, as irradiation increases. Chemical alteration of this material and its rod material, such as hydriding, is also likely, as are high temperature gradients and diffusion. For example, lithium mobility in lithium aluminate tends to in-

crease as lattice damage from irradiation increases, which either adversely or beneficially affects processes depending on the application [11]. Temperature gradients have also been postulated to play a large role in tritium diffusion processes. Other effects such as diffusion into grain boundaries are likely.

These effects, while not exhaustive, give a decent idea of the integral effects that are responsible for drastic changes in the material throughout its operational lifetime. In general, most of these effects are also responsible for a degradation in thermal performance by increasing resistance; impeding heat transport at the micro-scale. In general, these effects are often quantified as a function of material burn-up in nuclear fuels. Although less straightforward, the same can be done for lithium aluminate. Previous attempts to characterize the thermal performance of this material during irradiation have largely been empirical and not based on first principles. While empirical trends are helpful, first principles simulations may yield more detailed phenomenological information.

One particular observed effect during previous cycles of irradiation of TPBARs was extraneous tritium release, which in this case conflicts with the goals of the particular application. In general, the predictions of tritium release in the first cycle, shown in Figure 2, tended to be much lower than what was measured.

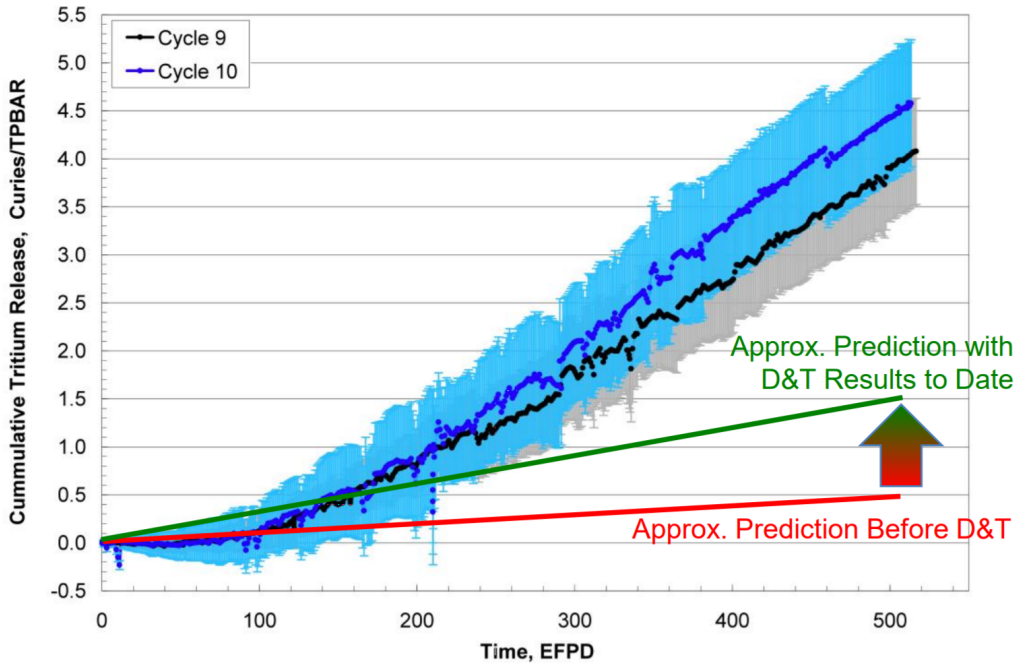

Figure 2: Tritium release prediction and actual tritium release vs. expected full power days (EPFD).

Observation of larger than expected tritium release and subsequent desire to understand the underlying mechanisms which ultimately affect the thermal performance and tritium transport in TPBARs led to the creation of the Tritium Science and Technology Program (TTP), overseen by Pacific Northwest National Laboratory (PNNL). The program's main effort is to create a multi-physics model of the TPBAR performance. This model, demonstrated in Figure 3, links multiple physics modules together such as phase field evolution, thermal transport, gaseous diffusion, *et cetera*. In the integrated modeling roadmap created by the TTP program, shown in Figure 3, thermal conductivity modeling directly provides inputs directly to the phase field modeling and

vice versa.

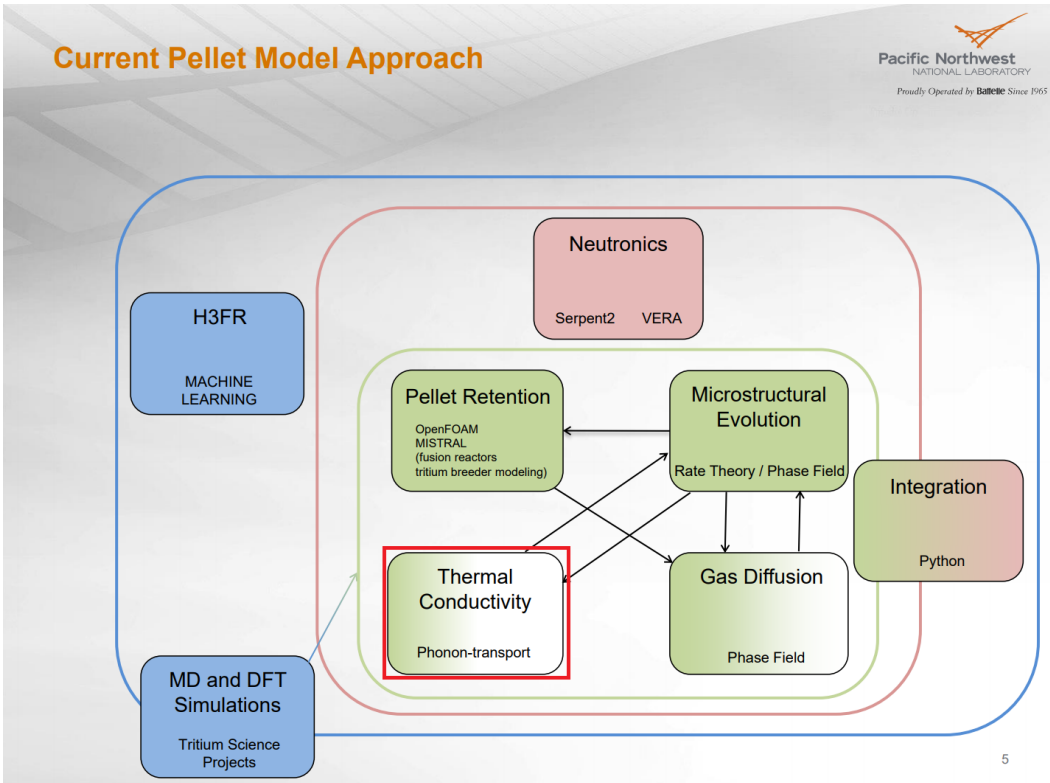

Figure 3: Integrated modeling road map created by the TTP program [12].

1.3 Purpose and scope of this work

This work aims to develop a first-principles based model of predicting thermal transport by modeling phonon physics using data informed from *ab initio* molecular dynamics and cluster dynamics calculations. It is expected that irradiation effects can be handled through the molecular dynamics calculations and the heterogeneity on the macro-scale (grain scale to engineering scale) can be handled spatially in the phonon physics module by altering phonon mean-free-path.

The first priority of this work is to provide inputs to the phase field model which is developed by PNNL. For example, some of the inputs desired as an output of this work are:

- Thermal conductivity of unirradiated lithium aluminate versus temperature over some operational range 300 - 1000 K
- Thermal conductivity of lithium aluminate with defects versus temperature over some operational range 300 - 1000 K
- Thermal conductivity of unirradiated lithium pentaluminate versus temperature over some operational range 300 - 1000 K
- Thermal conductivity of lithium pentaluminate versus temperature over some operational range 300 - 1000 K
- Thermal conductivity of the grain boundary between lithium aluminate and lithium pentaluminate over some operational range 300 - 1000 K

This work also aims to develop a spectrally and temperature dependent phonon transport solver which can compute thermal conductivity for micro-scale simulations, both modeling both perfect crystalline structures and irradiated structures with the option of handling boundaries as efficiently and accurately as possible, while exploring the performance and accuracy of methodologies required to do so.

2 RESEARCH OBJECTIVES

In general, three main research objectives are listed. Listed below each main objective are sub-objectives which aim to answer fundamental research questions at each phase of work.

2.1 Grey phonon transport

(Complete) Utilizing the Modular Finite Element Methods Library (MFEM), a free, lightweight, scalable `C++` library for finite element methods, demonstrate the capability of solving the Self-Adjoint Angular Flux (SAAF) formulation of the Single Relaxation Time (SRT) Grey phonon radiative transport (PRT) equation to obtain associated heat transfer quantities such as phonon radiance, temperature, heat flux, and thermal conductivity in the perfect crystal (homogeneous media).

- (Complete) Build upon the phonon transport computational framework by demonstrating the ability to solve the SAAF using higher order (HO) finite elements and the option of utilizing meshes with curved surfaces, verifying solutions through analytical comparisons (uniform infinite medium and purely absorbing source problems).
- (Complete) Quantitatively demonstrate spatial convergence rates of the SAAF formulation in MFEM using the Method of Manufactured Solutions (MMS) in cartesian meshes with straight edges and with curved edges.
- (Complete) Demonstrate the ability to computationally predict of temperature profiles in various materials by solving the SAAF SRT PRT, comparing solutions to existing literature.

- (Complete) Publication of above in review (attached in Appendix).

2.2 Homogeneous temperature and frequency dependent phonon transport

(In progress) Demonstrate the ability to perform frequency and temperature dependent phonon transport using the linearized SAAF-SRT-PRT in a perfect crystal (homogeneous media).

- (In progress) Develop and implement the frequency-dependent SAAF SRT PRT using the linearized temperature iteration scheme.
- (Incomplete) Demonstrate qualitatively the applicability of pseudo-scattering source iteration acceleration using DSA in the linearized temperature iteration scheme.
- (Incomplete) Demonstrate temperature profiles and thermal conductivity for test problems in literature and expand on knowledge base for lithium aluminate and lithium pentaluminate test problems.
- (In progress) Publication of above. Contributed summary submitted to ANS M&C 2020. Full paper submission expected in special issue of either *Nuclear Science and Engineering* or *Nuclear Engineering and Technology* in early 2021.

2.3 Heterogeneous temperature and frequency-dependent phonon transport

(Incomplete) Demonstrate the ability to perform frequency and temperature phonon transport in imperfect materials (heterogeneous media), such as a grain

boundary by using the order parameter method. The heterogeneities may include, but are not limited to, the lithium pentaluminate phase ($LiAl_5O_8$), grain boundaries, and voids (which may be handled as a modification of mean free path, rather than geometrically including these effects, depending on the problem scale).

- (In progress) Develop frequency and temperature dependent SAAF form of the phonon transport equation with order parameter function.
- (Incomplete) Model grain boundary thermal conductivity by combining lithium aluminate and lithium pentaluminate using the order parameter method in a heterogeneous test problem.
- (Incomplete) Develop method for coupling order parameters informed from phase field models to obtain a solution of the SAAF-SRT-PRT and predict thermal conductivity.
- (Incomplete) Publication of above.

2.4 Possible difficulties with research objectives

Obtaining data for frequency and temperature dependent properties lithium pentaluminate, as well as other atomistic effects in both lithium aluminate and lithium pentaluminate, depend on a tight coupling between this research and the molecular dynamics research.

Currently, there is data for lithium aluminate in the angle-frequency domain created in unison with our collaborators at University of California - Riverside. We currently do not have data for lithium pentaluminate, which is needed to satisfy the objectives laid out in Sec. 2.3.

Additionally, difficulty may arise in the coupling of phonon transport (boundary scattering) between two materials, such as in our case with lithium aluminate and lithium pentaluminate. We anticipate that the order parameter method will satisfy this requirement. Preliminary testing in the grey formulation has shown promise.

3 PROPOSED METHOD

3.1 Grey phonon transport

This section outlines the methods required to satisfy the main objective listed in Sec. 2.1.

3.1.1 Continuum phonon transport physics

In this section, we outline the integral Boltzmann phonon transport equations. We start from the general Boltzmann transport equation for phonons, and outline the approximations made to reach the formulations used in this work.

Phonons represent a quantized excitation in the vibrational modes in a solid. Often phonons are treated as particles rather than waves and are therefore designated as a quasi-particle. The treatment of phonons as quasi-particles allows for individual treatment in Monte Carlo or bulk treatment in deterministic transport simulations.

The Boltzmann phonon transport equation is governed by Eq. 1

$$\frac{\partial f}{\partial t} + \boldsymbol{v} \cdot \nabla \boldsymbol{f} = \left(\frac{\partial f}{\partial t}\right)_{collision}, \tag{1}$$

where the phonon distribution, $f = f(\boldsymbol{r}, \omega, \boldsymbol{\Omega}, p, t)$, is a function of position ($\boldsymbol{r}$), angular frequency (ω), direction ($\boldsymbol{\Omega}$), polarization (p), and time (t); the right-hand side of Eq. 1 describes the rate of change in phonon population due to collision events. The phonon velocity

$$\boldsymbol{v}(\omega, p) = \frac{\partial \omega(\boldsymbol{k}, p)}{\partial \boldsymbol{k}}, \tag{2}$$

is the gradient of ω in wavevector $\boldsymbol{k}$ space obtained through the phonon dispersion relation. The number density of phonons is given by

$$N(\boldsymbol{r},t) = \sum_p \int_0^{\omega_{max}} d\omega \int_{4\pi} d\boldsymbol{\Omega}\ f(\boldsymbol{r},\omega,\boldsymbol{\Omega},p,t)\frac{D(\omega,p)}{4\pi}, \tag{3}$$

where $D(\omega,p)$ is the phonon density of states when spherical symmetry is assumed:

$$D(\omega,p)f(\boldsymbol{r},\omega,\boldsymbol{\Omega},p,t)\frac{d\omega d\boldsymbol{\Omega}}{4\pi} = f(\boldsymbol{r},\boldsymbol{k},p,t)\frac{d^3\boldsymbol{k}}{(2\pi)^3}. \tag{4}$$

The phonon energy density is defined as

$$E(\boldsymbol{r},t) = \sum_p \int_0^{\omega_{max}} d\omega \int_{4\pi} d\boldsymbol{\Omega}\ \hbar\omega f(\boldsymbol{r},\omega,\boldsymbol{\Omega},p,t)\frac{D(\omega,p)}{4\pi}, \tag{5}$$

and the heat flux is given by

$$\boldsymbol{q}(\boldsymbol{r},t) = \sum_p \int_0^{\omega_{max}} d\omega \int_{4\pi} d\boldsymbol{\Omega}\ \hbar\omega\boldsymbol{v} f(\boldsymbol{r},\omega,\boldsymbol{\Omega},p,t)\frac{D(\omega,p)}{4\pi}. \tag{6}$$

Since energy is conserved in the collision of phonons, the properties of the right hand side of Eq. (1) imply that

$$\sum_p \int_0^{\omega_{max}} d\omega \int_{4\pi} d\boldsymbol{\Omega}\ \hbar\omega\frac{D(\omega,p)}{4\pi}\left(\frac{\partial f}{\partial t}\right)_{collision} = 0. \tag{7}$$

Since the basic phonon properties and governing equations have now been defined, we will now discuss the simplifications and assumptions applied in this work.

The right-hand side of Eq. 1, the time rate of change of the phonon distribution due to collisions, is commonly simplified by using the Single Mode Relaxation Time (SMRT) approximation:

$$\left(\frac{\partial f}{\partial t}\right)_{collision} = \frac{f^0 - f}{\tau} \tag{8}$$

where $\tau(\omega, p, T)$ is the relaxation time, T is temperature, and where

$$f^0(\omega, T) = n_{BE} = \frac{1}{e^{\frac{\hbar\omega}{k_B T}} - 1} \tag{9}$$

n_{BE} is the Bose-Einstein distribution [13, 14]. In the single mode relaxation time (SMRT) approximation, Eq. (1) becomes

$$\frac{\partial f}{\partial t} + \boldsymbol{v} \cdot \boldsymbol{\nabla} f = \frac{f^0 - f}{\tau} \tag{10}$$

The property of the right hand side of Eq.(1) with Eq. (7) leads to

$$\sum_p \int_0^{\omega_{max}} d\omega \int_{4\pi} d\boldsymbol{\Omega}\ \hbar\omega \frac{D(\omega, p)}{4\pi} \left(\frac{f^0 - f}{\tau}\right) = 0 \tag{11}$$

thus leading to the implicit energy balance relationship

$$\sum_p \int_0^{\omega_{max}} d\omega \int_{4\pi} d\boldsymbol{\Omega}\ \hbar\omega \frac{D(\omega, p)}{4\pi} \frac{f^0}{\tau} = \sum_p \int_0^{\omega_{max}} d\omega \int_{4\pi} d\boldsymbol{\Omega}\ \hbar\omega \frac{D(\omega, p)}{4\pi} \frac{f}{\tau}, \tag{12}$$

which is a constraining equation which must be applied in the solution of the equilibrium Boltzmann phonon transport equation.

It is more convenient in the modeling of heat transport to use the term angular phonon radiance I, or the intensity of phonons traveling in a given direction $\boldsymbol{\Omega}$, defined as

$$I(\boldsymbol{r}, \omega, \boldsymbol{\Omega}, p, t) = |\boldsymbol{v}| \hbar \omega D(\omega, p) f(\boldsymbol{r}, \omega, \boldsymbol{\Omega}, p, t) \tag{13}$$

and follows from the Boltzmann transport equation in Eq. 1. The time-dependent phonon radiative transport equation (PRT) following from the SMRT approximation in Eq. 10 is

$$\frac{1}{v}\frac{\partial I(\boldsymbol{r}, \omega, \Omega, p)}{\partial t} + \boldsymbol{\Omega} \cdot \boldsymbol{\nabla} I(\boldsymbol{r}, \omega, \Omega, p) = \frac{I^0(\omega, p, T) - I(\boldsymbol{r}, \omega, \Omega, p)}{\Lambda(\omega, p, T)}, \tag{14}$$

where the relaxation length, Λ, is defined in terms of the relaxation time and velocity as

$$\Lambda(\omega, p, T) = v\tau(\omega, p, T). \tag{15}$$

The heat flux in Eq. 6, written in terms of the angular phonon radiance, is now given by

$$\boldsymbol{q}(\boldsymbol{r}, t) = \frac{1}{4\pi}\int_0^{\omega_{max}} d\omega \int_{4\pi} d\boldsymbol{\Omega}\ \boldsymbol{\Omega} I(\boldsymbol{r}, \omega, \boldsymbol{\Omega}, p, t) \tag{16}$$

or the 1st angular moment of the angular phonon intensity I. We now assume steady-state in the time-dependent SRT-PRT equation in Eq. 14 by setting the partial derivative of the angular phonon intensity I with respect to time equal to zero, leading to the steady state, single mode relaxation time, phonon radiative transport (SRT-PRT) equation

$$\boldsymbol{\Omega} \cdot \boldsymbol{\nabla} I(\boldsymbol{r}, \omega, \Omega, p) + \frac{I(\boldsymbol{r}, \omega, \Omega, p)}{\Lambda(\omega, p, T)} = \frac{I^0(\omega, p, T)}{\Lambda(\omega, p, T)}. \tag{17}$$

3.1.2 Grey phonon transport approximation

Eq. 17 must still be solved subject to the constraint of energy conservation in Eq. 12. One approach to achieve this is to assume that phonon collisions only redistribute phonons to different directions, not to different frequencies. All scattering is also treated as elastic, and there is no coupling between the phonon populations at different frequencies. This approximation allows one to model the transport of phonons at each frequency individually as a *grey* population of phonons with the same mean free path and velocity. Modeling phonon populations as grey assumes that the entire Brillouin zone is represented by one singular phonon velocity and relaxation time [15].

The constraint in Eq. 12 becomes trivial if all phonon frequencies and polarizations experience the same mean free path, or if the transport properties are averaged over frequency and polarization to consider only a *grey* population of phonons with the same averaged frequency, velocity, and effective mean free path. As a stepping stone to modeling the full frequency dependent case, in the remainder of this section we restrict our attention to this grey test case. The grey approximation can also be used as a comparison to the kinetic theory approximation, which will be described later.

In this section, we describe our approach to collapse the number of frequencies and polarizations to one effectively homogeneous grey phonon group which is independent or constant in frequency, polarization, and temperature. Although less physically valid, the grey treatment makes verification of the implementation of the numerical solution much easier. The grey approximation can

also be used as a comparison to the kinetic theory approximation, which will be described later. In later sections, multi-frequency, temperature dependent phonon transport will be considered.

We also assume that the number of polarizations, p, is equal to one. We assume that the continuum integral over frequency, ω, can be collapsed to a singular discrete frequency group over the singular polarization. Additionally, the phonon mean free path Λ, is assumed to be constant. These assumptions are typical in previous work.

We introduce the scalar phonon radiance, ϕ, which is defined as

$$\phi(\boldsymbol{r}) = \int_{4\pi} d\boldsymbol{\Omega}\ I(\boldsymbol{r}, \boldsymbol{\Omega}) \tag{18}$$

or simply the 0th angular moment of the angular phonon radiance. We similarly define an equilibrium scalar phonon radiance, ϕ^0, which is a function of system temperature, T,

$$\phi^0(\boldsymbol{r}, T) = \int_{4\pi} d\boldsymbol{\Omega}\ I^0(\boldsymbol{r}, \boldsymbol{\Omega}, T). \tag{19}$$

We make the following simplification that the scalar phonon radiance is isotropic, or that the phonon properties in on crystallographic direction are representative of the entire Brillouin zone:

$$\frac{\phi(\boldsymbol{r})}{4\pi} = I(\boldsymbol{r}, \boldsymbol{\Omega}). \tag{20}$$

The final approximation we make is that the scalar equilibrium phonon radiance is equal to the scalar phonon radiance, such that

$$\phi^0 = \phi \tag{21}$$

Under these simplifications, Eq. 17 becomes

$$\boldsymbol{\Omega} \cdot \boldsymbol{\nabla} I(\boldsymbol{r}, \boldsymbol{\Omega}) + \frac{I(\boldsymbol{r}, \boldsymbol{\Omega})}{\Lambda} = \frac{I^0(\boldsymbol{r}, \boldsymbol{\Omega})}{\Lambda}. \tag{22}$$

The iterative solution of Eq. (22) will be described in the Methods section.

3.1.3 Heat transfer relations

Our assumptions thus far have yet to include the relation needed to obtain temperature information from a given equilibrium scalar phonon radiance ϕ^0. The final relation needed to iterate between the angular phonon radiance, scalar phonon radiance, and temperature is

$$CvT = \phi^0(\boldsymbol{r}, T), \tag{23}$$

where C is the volumetric heat capacity, and v is the phonon group velocity [16]. The product of the volumetric heat capacity and the temperature, CT can be viewed as the thermal energy in the system, and v is the velocity at which it is propogating.

By solving for the steady-state scalar-equilibrium phonon radiance, the temperature T is obtained from Eq. 23. The solution for the global temperature, obtained by inverting Eq. 23 for T, can be used to compute the temperature gradient, $\boldsymbol{\nabla} T(\boldsymbol{r})$.

Similar to the method used to compute the scalar phonon radiance in Eq. 18, the heat flux is

$$\boldsymbol{q}(\boldsymbol{r}) = \int_{4\pi} d\boldsymbol{\Omega}\ \boldsymbol{\Omega} I(\boldsymbol{r}, \boldsymbol{\Omega}), \tag{24}$$

or the 1st angular moment of the angular phonon radiance over the 4π unit sphere.

In most phonon transport studies, the thermal conductivity is obtained by computing domain averaged quantities. While Fourier's law applies in certain length scales and it does not necessarily make sense to apply it in an infinitesimal limit, it can serve as a useful comparison. Fourier's Law relates the heat flux, $\boldsymbol{q}(\boldsymbol{r})$, to the temperature gradient $\boldsymbol{\nabla} T(\boldsymbol{r})$ by the thermal conductivity, k as

$$\boldsymbol{q}(\boldsymbol{r}) = -k \boldsymbol{\nabla} T(\boldsymbol{r}). \tag{25}$$

and can be viewed as a diffuse treatment of heat transport. Comparisons against Fourier's Law will determine where diffuse treatment can be expected. In this work, the thermal conductivities reported use an infinitesimal representation of Fourier's Law, rather than using domain averaged quantities.

In anisotropic materials, such as thin films or laminated materials, thermal conductivity can be considered a tensor which depends on the crystallographic orientation. In this work, we assume that the entries in the N-dimensional tensor are simply on the diagonal, allowing for directional separation, which is a typical assumption for these simulations. Periodic boundary conditions on both y-direction boundaries, y = 0 and y = 1 in this case, in a 2-dimensional simulation on the xy-plane allow for an effectively one-dimensional simulation of phonon transport. The handling of the simulation domain and use isothermal boundaries is similar to that used in work by Mittal and Mazumder [17].

The negative quotient of the dot product of both the heat flux and the temperature gradient into the x-direction yield the thermal conductivity in a Fourier's law representation in the x-direction, respectively. This method will be described in greater detail in Section 5.1.2 by using an illustration in Fig. 11.

$$k_{\boldsymbol{x}} = -\frac{\boldsymbol{q} \cdot \hat{\boldsymbol{x}}}{\boldsymbol{\nabla} T \cdot \hat{\boldsymbol{x}}} \tag{26}$$

As a comparison to the our results of the Boltzmann transport simulations of phonons, we employ the use of the kinetic theory representation of the thermal conductivity

$$k = \frac{\Lambda}{3} C v, \tag{27}$$

which computes the thermal conductivity from the mean free path, heat capacity, and velocity of the heat carrier, or phonon in this case [16, 18].

3.1.4 Self-adjoint angular flux formulation of the SRT-PRT

In this work, we employ the Self-Adjoint Angular Flux (SAAF) formulation of the phonon radiative transport equation in Eq. 22. The spatially first-order Boltzmann phonon transport equation, Eq. 22, is a hyperbolic equation, whereas the SAAF formulation yields a set of spatially second-order, elliptic equations. The SAAF formulation offers several advantages over the spatially first-order radiative transport equation, some of which we will briefly discuss [19]. The SAAF formulation allows for usage of the continuous finite element spatial discretization (CFEM), rather than the discontinuous finite element method (DFEM) which is often used to stabilize the first-order form of

the transport equation. CFEM discretizations often result in symmetric positive definite (SPD) matrices, which can be solved with the iterative conjugate gradient (CG) method.

Although there are multiple ways to derive the Self-Adjoint Angular Flux equation, we follow a simple algebraic derivation outlined by Morel and McGhee [20]. We first begin with the continuum steady-state SRT-PRT equation in Eq. 17. We now represent the angular phonon radiance I in terms of the streaming operator $\Lambda\boldsymbol{\Omega}\cdot\boldsymbol{\nabla}I$ and angular equilibrium phonon radiance I^0 as

$$I = I^0 - \Lambda\boldsymbol{\Omega}\cdot\boldsymbol{\nabla}I, \tag{28}$$

and substitute the right hand side of Eq. 28 for I in the streaming operator $\Lambda\boldsymbol{\Omega}\cdot\boldsymbol{\nabla}I$ back into Eq. 17 and dividing by Λ to obtain the SAAF-SRT-PRT equation

$$-\boldsymbol{\Omega}\cdot\boldsymbol{\nabla}(\Lambda\boldsymbol{\Omega}\cdot\boldsymbol{\nabla}I) + \frac{I}{\Lambda} = \frac{I^0}{\Lambda} - \boldsymbol{\Omega}\cdot\boldsymbol{\nabla}I^0. \tag{29}$$

3.1.5 Discrete ordinates (S_N) angular discretization

In this work, the angular variable is discretized using the discrete ordinates (S_N) method, which subdivides the 4π solid angle unit sphere into a set of discrete angular vectors $[\boldsymbol{\Omega}_1, .., \boldsymbol{\Omega}_N]$ and associated weights $[w_1, .., w_N]$, where N is the angular order. The combined set of angles $\boldsymbol{\Omega}_n$ weights w_n is referred to the angular quadrature set. In this work, the S_8 Level-Symmetric (LQ_N) quadrature set is used.

We omit discussion of the advantages and disadvantages of quadrature selection outside of mentioning that certain quadrature sets are more attractive

depending on the the unique problem selection. The choice of specific quadrature and angular expansion order in the grey transport of phonons is less crucial due to the purely scattering nature of phonon physics, as purely scattering media is not prone to ray effects found in discrete ordinates simulations of optically thin media, such as a vacuum.

Using the grey approximation the continuous angular integrals can now be written as single discrete summation over the ordinates. Using this method we assume that the scalar phonon radiance $\phi(\boldsymbol{r})$, for example, can be reconstructed by a discrete summation multiplying the angular phonon radiance $I_n(\boldsymbol{r}, \Omega_n)$ in each angular ordinate by its respective weight w_n

$$\phi(\boldsymbol{r}) = \int_{4\pi} d\boldsymbol{\Omega}\ I(\boldsymbol{r}, \boldsymbol{\Omega}) \longrightarrow \sum_N I_n(\boldsymbol{r}, \boldsymbol{\Omega}_n) w_n(\boldsymbol{\Omega}_n). \tag{30}$$

The discrete heat flux calculation is similar to that as in Eq. 30 with the inclusion of the direction vector $\boldsymbol{\Omega}$. For example, the heat flux in the x-direction is simply:

$$\boldsymbol{q}_x(\boldsymbol{r}) = \int_{4\pi} d\boldsymbol{\Omega}\ |\boldsymbol{\Omega} \cdot \boldsymbol{x}| I(\boldsymbol{r}, \boldsymbol{\Omega}) \longrightarrow \sum_N \mu_n(\boldsymbol{\Omega}_n) I_n(\boldsymbol{r}, \boldsymbol{\Omega}_n) w_n(\boldsymbol{\Omega}_n), \tag{31}$$

3.1.6 Finite element spatial discretization

In this work, we spatially discretize the SAAF-SRT-PRT in Eq. 29 using the finite element method through the MFEM software package. MFEM is a scalable and modular finite element library written in `C++` and offers the ability to use arbitrarily higher-order finite elements on unstructured meshes with or without curved surfaces [21]. Previous work by Woods has successfully demonstrated the solution of the spatially first-order form of the neutron transport in

MFEM, analogous to the SRT-PRT phonon transport equation in Eq. 22, using higher-order discontinuous finite elements (DFEM) on meshes with curved surfaces [22, 23, 24]. In this work, however, the continuous finite element discretization (CFEM) is used to spatially discretize the SAAF-SRT-PRT equation, which is considered to be spatially second order.

Following the derivation by Wang, Zong, and Martineau [25] which outlines the CFEM finite element formulation for the SAAF neutron transport equation, the SAAF-SRT-PRT is written in the weak form using similar notation for volume and surface integrals.

$$\begin{aligned}(\boldsymbol{\Omega}\cdot\boldsymbol{\nabla}I^*, \Lambda\boldsymbol{\Omega}\cdot\boldsymbol{\nabla}I)_D + (I^*, \frac{I}{\Lambda})_D + \ < I^*, I >_{\delta D^+} = \\ (I^* + \Lambda\boldsymbol{\Omega}\cdot\boldsymbol{\nabla}I^*, I^0)_D + < I^*, I_{inc} >_{\delta D^-} \ .\end{aligned} \tag{32}$$

In Eq. 32, I^* represents the basis function, and I represents the test function. The notation for the inner products over the domain D are

$$(I^*, I)_D \ = \int_D I^*(\boldsymbol{\Omega}, \boldsymbol{r}) I(\boldsymbol{\Omega}, \boldsymbol{r}) \ d\boldsymbol{r}, \tag{33}$$

and the notation for inner products over the domain surface δD are

$$< I^*, I >_{\delta D} \ = \int_{\delta D} |\boldsymbol{\Omega}\cdot\hat{\boldsymbol{n}}| I^*(\boldsymbol{\Omega}, \boldsymbol{r}) I(\boldsymbol{\Omega}, \boldsymbol{r}) \ d\boldsymbol{S} \tag{34}$$

The inner products over the surface of the domain in Eq. 32 are split into two separate inner products which include either a negative or positive superscript on δD and denote whether the term is for inflow or outflow boundaries respectively. Inflow boundaries are specified on the condition $\boldsymbol{\Omega}\cdot\hat{\boldsymbol{n}} < 0$ and

constitute the implementation of the Dirichlet boundary conditions and use Eq. 23 to define the incident angular phonon radiance

$$I_{inc} = \frac{CvT(\boldsymbol{r}_b)}{4\pi}, \tag{35}$$

where $T(\boldsymbol{r}_b)$ is the boundary temperature. Additionally, the outflow boundaries are specified by the condition $\boldsymbol{\Omega} \cdot \hat{\boldsymbol{n}} \geq 0$. The inflow boundary condition — which is typically the only condition required in the spatially first-order discretization — *and* the outflow boundary condition are both required for closure in the SAAF spatial discretization. Since the outflow inner product is unknown, it appears on the left hand side of Eq. 32. In the CFEM formulation interior neighbor surfaces are canceled, thus the outflow condition will only appear on the boundary of the entire domain.

Each term in the weak form of the SAAF-SRT-PRT in Eq. (32) was implemented by the following standard MFEM bilinear or linear terms in Table 1.

3.1.7 Grey iterative solution methodology

We use the standard source iteration technique for numerically solving the SAAF-SMRT-PRT equation [26]. We assume an initial distribution for the scalar phonon radiance ϕ, and solve for an updated ϕ which is then used on the next iteration, or lagged. This iterative solution methodology is outlined in Algorithm 1.

The spectral radius ρ, which is bounded between 0 and 1, is a measure of the rate of convergence of the error in the iterative method. In the context of our iterative methodology, the spectral radius is estimated in terms of the l_∞ norm

Table 1: MFEM bilinear and linear forms.

Weak Form	Integrator Form	Integrator Type	MFEM Form Name
$(\mathbf{\Omega} \cdot \boldsymbol{\nabla} I^*, \Lambda \mathbf{\Omega} \cdot \boldsymbol{\nabla} I)_D$	Bilinear	Domain	**DiffusionIntegrator**
$(I^*, \frac{I}{\Lambda})_D$	Bilinear	Domain	**MassIntegrator**
$< I^*, I >_{\delta D^+}$	Bilinear	Surface	**DGTraceIntegrator**
$(I^*, I^0)_D$	Linear	Domain	**DomainLFIntegrator**
$(\Lambda \mathbf{\Omega} \cdot \boldsymbol{\nabla} I^*, I^0)_D$	Linear	Domain	***Custom**
$< I^*, I_{inc} >_{\delta D^-}$	Linear	Surface	**BoundaryFlowIntegrator**

of the differences between scalar phonon radiances between iterations, l, as

$$\rho^{(l)} = \frac{|\phi^{(l+1)} - \phi^{(l)}|_\infty}{|\phi^{(l)} - \phi^{(l-1)}|_\infty}. \tag{36}$$

An implication of the iterative solution methodology is that to reach a tolerance ϵ, the number of iterations n required will at least be such that $\rho^n < \epsilon$. The source iteration continues until the differences between the iterates of the scalar phonon radiance, ϕ, are less than some predefined tolerance. For convenience, we define the L_∞ norm of the difference of the scalar phonon radiance estimates as

$$\Delta^{(l)} = |\phi^{(l+1)} - \phi^{(l)}|_\infty, \tag{37}$$

Our convergence criterion is defined as met when the following holds true:

$$\Delta^{(l)} < \epsilon \times (1 - \rho^{(l)}) \times |\phi^{(l)}|_\infty. \tag{38}$$

Algorithm 1 Grey Phonon Transport Source Iteration

Guess $\phi^{0^{(0)}}, I^{0^{(0)}}$

Tolerance $\epsilon = 10^{-8}$

Iterate count $l = 0$

while $\Delta^{(l)} > \epsilon \times (1 - \rho^{(l)}) \times |\phi^{(l)}|_\infty$ **do**

  for $\boldsymbol{\Omega}_n$ *in* $\boldsymbol{\Omega}$ **do**

    $-\boldsymbol{\Omega}_n \cdot \boldsymbol{\nabla}[\Lambda \boldsymbol{\Omega}_n \cdot \boldsymbol{\nabla} I^{(l+1)}] + \frac{I^{(l+1)}}{\Lambda} = -\boldsymbol{\Omega}_n \cdot \boldsymbol{\nabla} I^{0,(l)} + \frac{I^{0,(l)}}{\Lambda}$

  end

  $\phi^{(l+1)} = \sum_N w_n I_n^{(l+1)}$

  $I^{0,(l+1)} = \frac{1}{4\pi}\phi^{(l+1)}$

  $\rho^{(l)} = \frac{|\phi^{(l+1)} - \phi^{(l)}|_\infty}{|\phi^{(l)} - \phi^{(l-1)}|_\infty}$

  $\Delta^{(l)} = |\phi^{(l+1)} - \phi^{(l)}|_\infty$

  $l = l + 1$

end

$\boldsymbol{q} = \sum_N \boldsymbol{\Omega_n} I_n^{(l)} w_n$

$T = \frac{\phi^{(l)}}{Cv}$

$k_x = \frac{-\boldsymbol{q_x}}{\boldsymbol{\nabla T_x}}$

Now that we have described a general approach for implementing a grey, or 1-group frequency independent phonon transport methodology we will now outline our approach for the solution of frequency and temperature dependent phonon transport.

3.2 Temperature and frequency dependent phonon transport

This section outlines the methods required to satisfy the main objective listed in Sec. 2.2 and part of the main objective listed in Sec. 2.3.

The outline of the frequency, and temperature dependent methodology was made with the assistance of an outline provided by Dr. Dmitriy Anistratov at N.C. State University [27].

In general, many of the assumptions and methodologies laid out in the previous section, such as the SMRT approximation, the SAAF formulation, and the finite element spatial discretization are retained. Any deviations from the previous approach will be noted.

3.2.1 Description of temperature and frequency dependent approach

The approach to the non-linear coupling between the phonon intensity and the material temperature is motivated by a mature algorithm used in the thermal radiation transport community, which employs a Newton iteration on the non-linear dependence of the Planck function on material temperature. In this application, the temperature and the phonon emission are constrained through the non-linear Bose-Einstein distribution.

The approach uses the phonon transport equation presented earlier but with an added term that couples the groups together via the current estimate of temperature. The addition of this term resembles a calculation of an absorption term with a simultaneous re-emission, justly referred to as "pseudo-scattering" iteration. This term is mathematically similar to what is seen in fission source iteration in neutron transport.

3.2.2 Frequency and temperature dependent phonon transport in the linearized approach

We return to the steady state SRT-PRT equation rewritten below

$$\boldsymbol{\Omega} \cdot \boldsymbol{\nabla} I(\boldsymbol{r}, \omega, \Omega, p) + \frac{I(\boldsymbol{r}, \omega, \Omega, p)}{\Lambda(\omega, p, T)} = \frac{I^0(\omega, p, T)}{\Lambda(\omega, p, T)}. \tag{39}$$

We now define the phonon emission term (PET), a material temperature dependent quantity, as

$$\tilde{W}^0(T) = \sum_p \int_0^{\omega_{max}} d\omega \frac{I^0(\omega, p, T)}{\Lambda(\omega, p, T)} \tag{40}$$

and the phonon scattering term (PST), a transport calculated quantity, as

$$\tilde{W}_s(T) = \sum_p \int_0^{\omega_{max}} d\omega \int_{4\pi} d\boldsymbol{\Omega} \frac{I(\boldsymbol{r}, \omega, \boldsymbol{\Omega}, p)}{\Lambda(\omega, p, T)}. \tag{41}$$

The energy balance relationship in Eq. 12 is now re-written in terms of the PET and PST as

$$\tilde{W}^0(T) = \tilde{W}_s(T). \tag{42}$$

We now lag the mean free path Λ in the steady state SRT-PRT in Eq. 39 by evaluating at temperature T^*

$$\boldsymbol{\Omega} \cdot \boldsymbol{\nabla} I(\boldsymbol{r}, \omega, \Omega, p) + \frac{I(\boldsymbol{r}, \omega, \Omega, p)}{\Lambda(\omega, p, T^*)} = \frac{I^0(\omega, p, T)}{\Lambda(\omega, p, T^*)}. \tag{43}$$

We now linearize the Bose-Einstein function in Eq. 9 such that we can now write Eq. 43 as

$$\boldsymbol{\Omega} \cdot \boldsymbol{\nabla} I(\boldsymbol{r}, \omega, \Omega, p) + \frac{I(\boldsymbol{r}, \omega, \Omega, p)}{\Lambda(\omega, p, T^*)} = \frac{1}{\Lambda(\omega, p, T^*)} \left[I^0(\omega, p, T^*) + \frac{\partial I^0}{\partial T}(\omega, p, T^*)(T - T^*) \right] \tag{44}$$

We also now lag the mean free path by temperature T^* in the PST in Eq. 42 such that at $T = T^*$

$$\tilde{W}^0(T) = \tilde{W}_s(T^*). \tag{45}$$

We also now linearize the PET in Eq. 45 around T^* to obtain

$$\tilde{W}^0(T^*) + (T - T^*)\frac{d\tilde{W}^0}{dT}|_{T=T^*} = \tilde{W}_s(T^*) \tag{46}$$

which leads us to an expression for the temperature increment based on the energy balance relationship

$$T - T^* = \left[\frac{d\tilde{W}^0}{dT}|_{T=T^*} \right]^{-1} (\tilde{W}_s(T^*) - \tilde{W}^0(T^*)). \tag{47}$$

Substituting the temperature increment from Eq. 47 into Eq. 44, and by defining

$$\gamma(\omega, p, T^*) = \left[\frac{d\tilde{W}^0}{dT}|_{T=T^*} \right]^{-1} \frac{\partial I^0}{\partial T}|_{T=T^*} \tag{48}$$

we obtain the linearized SRT-PRT with pseudo-scattering

$$\mathbf{\Omega} \cdot \boldsymbol{\nabla} I + \frac{I}{\Lambda(T^*)} = \frac{1}{\Lambda(T^*)} \left(I^0(T^*) - \gamma(T^*)\tilde{W}^0(T^*)) \right) + \frac{\gamma(T^*)}{\Lambda(T^*)} \tilde{W}_s(T^*) \tag{49}$$

We note that Eq. 49 is solved in each angle and is driven by a fixed angular source dependent *only* on temperature, $\frac{1}{\Lambda(T^*)} \left(I^0(T^*) - \gamma(T^*)\tilde{W}^0(T^*)) \right)$, and a transport driven quantity, $\frac{\gamma(T^*)}{\Lambda(T^*)} \tilde{W}_s(T^*)$, which changes each iteration. This deviates from the physics in the grey transport algorithm, and may slightly alleviate some of the numerical concerns posed with solving a purely scattering and boundary driven only transport problem.

In the inner iteration, where temperature does not change, the equation we are solving (with inner iterative index l) is:

$$\mathbf{\Omega_g} \cdot \nabla I_g^{(l+1)} + \frac{I_g^{(l+1)}}{\Lambda_g(T^*)} = [\frac{I_g^0(T^*) - \gamma_g(T^*)\tilde{W}^0(T^*)}{\Lambda_g(T^*)}] + \frac{\gamma_g(T^*)}{\Lambda_g(T^*)} \tilde{W}_s^{(l)} \tag{50}$$

3.2.3 Angular discretization and spectral mapping

In concert with molecular dynamics experts, we have developed a new approach which now deviates slightly from an angular quadrature seen in traditional S_N calculations. Instead, discrete angle-energy groups were chosen to represent the frequency dependence. The spectral and temperature dependent data set for lithium aluminate contains 130 separate angle-energy groups comprising of 26 angles and 5 different mean free paths per angle. Figure 4 represents the angular discretization, and Figure 5 illustrates the mean free path for each group.

Since $\Lambda_g(T)$, shown in Figure 5 for each group, is guaranteed to be positive

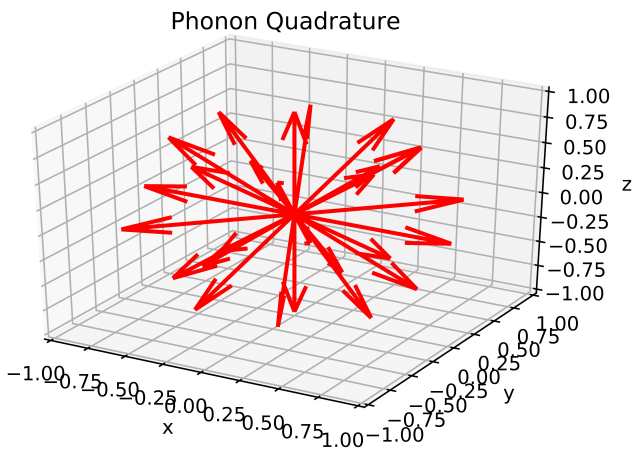

Figure 4: Molecular dynamics informed angular quadrature.

we expect that all of the γ_g *must* be positive over the temperature range we expect for any meaningful interpretation of physical data.

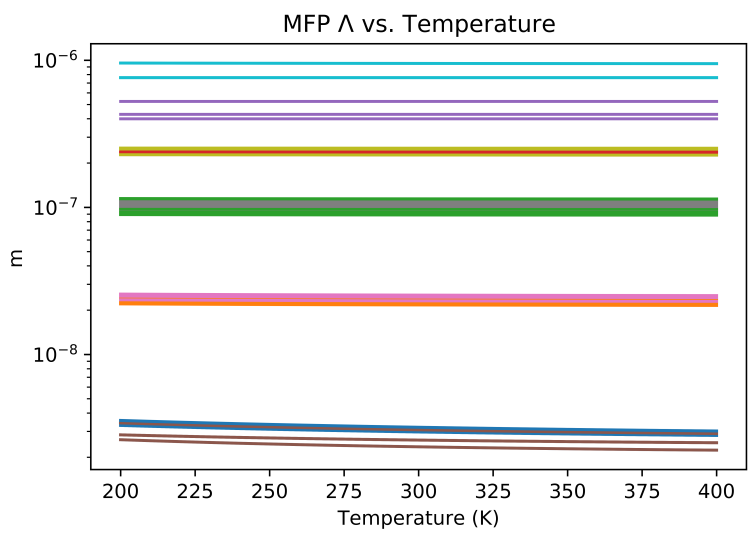

Figure 5: Mean free path vs. temperature for each angle-energy group.

Since γ_g was not included in the original data set, the term was calculated for each group using polynomial fits of terms provided, as shown in Figure 6.

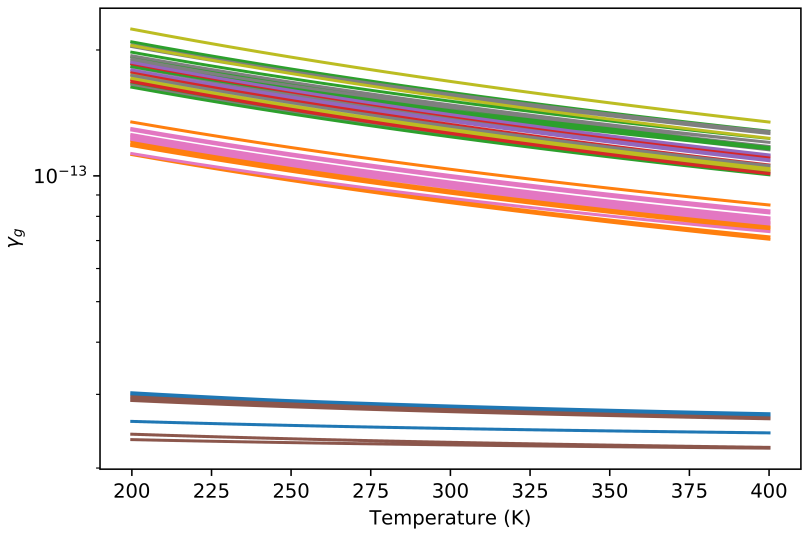

Figure 6: $\gamma_g(T)$ computed by taking quotient of two polynomial fits.

Instead of using a traditional weight determined by integrating a polynomial exactly, we now use weights determined by the molecular dynamics simulations. The heat flux is now computed by computing a discrete sum over the quadrature set and using prescribed weights from determining an angle-energy group's fractional contribution to the total heat flux at that temperature.

For example, the PST now is defined in terms of a discrete summation over transport computed properties as a function of temperature as

$$\tilde{W}_s(\mathbf{r}) = \sum_G A_g[T^*(\mathbf{r})]B_g[T^*(\mathbf{r})]I_g. \tag{51}$$

With this approach, spectrally dependent properties are computed while maintaining the same inner iteration structure as before with the grey approach but

at the cost of more angles and also iterating on material temperature.

An example of a set of five energy groups for a single angle is shown below in Table 2.

Table 2: Example quadrature, weighting, and Λ grouping in the frequency and temperature dependent approach.

Angle Energy Group	$\mathbf{\Omega}_x$	$\mathbf{\Omega}_y$	$\mathbf{\Omega}_z$	B_g	$\Lambda(m)$
1	0	0	1	3249	2.36E-09
2	0	0	1	100	2.32E-08
3	0	0	1	20	1.01E-07
4	0	0	1	8	2.27E-07
5	0	0	1	3	9.52E-07

3.2.4 Frequency and temperature dependent pseudo-scattering algorithm

By substituting the molecular dynamics informed discrete representations for the the temperature, PET, PST, and heat flux outlined in the previous section, we obtain an algorithm which retains frequency and temperature dependence in the calculation of transport properties. The algorithm used to solve the linearized temperature and frequency dependent phonon transport problem is shown below in Algorithm 2.

Algorithm 2 An iterative algorithm for solving frequency and temperature dependent deterministic phonon transport equation in the SAAF form

while $||\Delta T^{(\ell)}(\mathbf{r})||_\infty > \epsilon_T$ **do**

$\ell = \ell + 1$

while $||\Delta \tilde{W}_s^{(k,\ell)}(\mathbf{r})||_\infty > \epsilon_s$ **do**

$k = k + 1$

for $\mathbf{\Omega}_g$ *in* $\mathbf{\Omega}$ **do**

$$-\mathbf{\Omega}_g \cdot \nabla \left[\Lambda_g[T^{(\ell)}]\mathbf{\Omega}_g \cdot \nabla I_g^{(k+1,\ell)}\right] + \frac{1}{\Lambda_g[T^{(\ell)}]} I_g^{(k+1,\ell)} =$$
$$-\mathbf{\Omega}_g \cdot \nabla \left[I_g^0[T^{(\ell)}] - \gamma_g[T^{(\ell)}]\left(\tilde{W}^0[T^{(\ell)}] - \tilde{W}_s[T^{(\ell)}, I_g^{(k,\ell)}]\right)\right]$$
$$+\frac{1}{\Lambda_g[T^{(\ell)}]}\left[I_g^0[T^{(\ell)}] - \gamma_g[T^{(\ell)}]\left(\tilde{W}^0[T^{(\ell)}] - \tilde{W}_s[T^{(\ell)}, I_g^{(k,\ell)}]\right)\right]$$

end

$\tilde{W}_s^{(k+1,\ell)} = \sum_G A_g[T^{(\ell)}]B_g[T^{(\ell)}]I_g^{(k+1,\ell)}$

$\Delta \tilde{W}_s^{(k+1,\ell)} = \tilde{W}_s^{(k+1,\ell)} - \tilde{W}_s^{(k,\ell)}$

end

$\tilde{W}_s^{(\ell+1)} = \tilde{W}_s^{(k+1,\ell)}$

$I^{(\ell+1)} = I^{(k+1,\ell)}$

$T^{(\ell+1)} = T^{(\ell)} + \left(\frac{\partial \tilde{W}^0}{\partial T}|_{T=T^{(\ell)}}\right)^{-1}(\tilde{W}_s^{(\ell+1)} - \tilde{W}^0)$

$\Delta T^{(\ell+1)} = T^{(\ell+1)} - T^{(\ell)}$

end

$\hat{T} = T^{(\ell+1)}$

$\hat{I} = I^{(\ell+1)}$

$\mathbf{q} = \sum_G \mathbf{\Omega}_g \Gamma_g[\hat{T}]B_g[\hat{T}]\hat{I}_g$

$k_x = -\frac{1}{L}\int \frac{\mathbf{q}\cdot\hat{x}}{\nabla\hat{T}\cdot\hat{x}}\, dx$

3.3 Phonon transport with material heterogeneity, interfacial scattering

This section outlines the methods required to satisfy the main objective listed in Sec. 2.3.

Thus far the methodologies developed handle phonon transport in homogeneous materials. Boundary or interfacial scattering must be resolved in order to handle heterogeneous materials. In general, interfacial physics depend on the structure of the interface and the mismatch between the two materials. The boundary scattering phenomemenon in general is not well understood.

Recent approaches to handle boundary scattering by Harter *et al.* have used the diffuse mismatch model to quantify boundary scattering [28, 29]. We intend to take a new and different approach to handle boundary scattering physics.

3.3.1 Order parameter method for moving interfacial scattering into the grey BTE

Recent investigations into the boundary resistance formulation has led other researchers to move interfacial scattering into the Boltzmann transport equation itself [30]. Moving the interfacial scattering into the formulation requires a scalar field, named the order parameter (η), representing boundaries in phase fields and would arguably be a much more natural way to inform phonon transport calculations. An example of an order parameter field informed from a phase field model is shown in Figure 7.

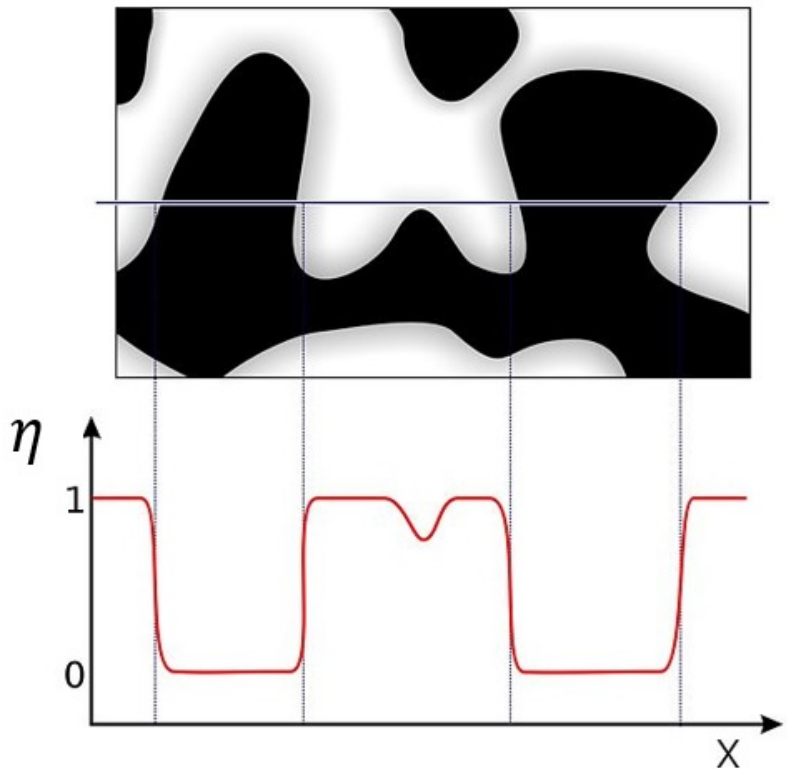

Figure 7: Order parameter informed from phase field modeling.

In order to derive the modification of the phonon BTE with the order parameter, we once again return our attention to the grey phonon transport equation in Eq. 17, and assume again the grey case and add an additional scattering term, α, such that:

$$\boldsymbol{\Omega} \cdot \boldsymbol{\nabla} I(\boldsymbol{r}, \boldsymbol{\Omega}) + \frac{I(\boldsymbol{r}, \boldsymbol{\Omega})}{\Lambda} = \frac{I^0(\boldsymbol{r}, T)}{\Lambda} + \alpha. \tag{52}$$

We now consider an interface at equilibrium with a uniform temperature T such that the equilibrium angular phonon radiance is equal to the angular phonon radiance:

$$I(\boldsymbol{r}, \boldsymbol{\Omega}) = I^0(\boldsymbol{r}, T). \tag{53}$$

Assuming the equilibrium angular radiance is material property as a function of temperature, and that the product of v_g and C_v is a function of order parameter:

$$I^0(\boldsymbol{r}, T, \eta) = \frac{[v_g C_v(\eta)]T}{4\pi}, \tag{54}$$

we can substitute I^0 for I in Eq. 52 to obtain:

$$\boldsymbol{\Omega} \cdot \boldsymbol{\nabla} I^0(\boldsymbol{r}, T, \eta) + \frac{I^0(\boldsymbol{r}, T, \eta)}{\Lambda} = \frac{I^0(\boldsymbol{r}, T.\eta)}{\Lambda} + \alpha. \tag{55}$$

Expanding the gradient of I^0 using Eq. 54 we obtain:

$$\boldsymbol{\Omega} \cdot \left(\frac{dI^0}{dT} \boldsymbol{\nabla} T + \frac{dI^0}{d[vC]} \boldsymbol{\nabla} [vC] \right) + \frac{I^0(\boldsymbol{r}, T)}{\Lambda} = \frac{I^0(\boldsymbol{r}, T)}{\Lambda} + \alpha. \tag{56}$$

Cancelling the temperature gradient, as the temperature is uniform, and cancelling the two identical terms, we obtain the scattering term as a function of the material property gradient

$$\alpha = \frac{dI^0}{d[vC]} \boldsymbol{\Omega} \cdot \boldsymbol{\nabla} [vC]. \tag{57}$$

Substituting α into Eq. 52, we obtain:

$$\boldsymbol{\Omega} \cdot \boldsymbol{\nabla} I(\boldsymbol{r}, \boldsymbol{\Omega}) + \frac{I(\boldsymbol{r}, \boldsymbol{\Omega})}{\Lambda} = \frac{I^0(\boldsymbol{r}, T)}{\Lambda} \left(1 + \frac{\Delta vC}{vC(\eta)} \boldsymbol{\Omega} \cdot \boldsymbol{\nabla} \eta(\boldsymbol{r}) \right) \tag{58}$$

The order parameter method is energy conserving due to the property

$$0 = \int_{4\pi} d\boldsymbol{\Omega} \left(\boldsymbol{\Omega} \cdot \boldsymbol{\nabla} \eta(\boldsymbol{r}) \right). \tag{59}$$

We note that the term $\left(1 + \frac{\Delta vC}{vC(\eta)} \boldsymbol{\Omega} \cdot \boldsymbol{\nabla} \eta(\boldsymbol{r})\right)$ that modifies the equilibrium scalar radiance on the right hand side of Eq. 58 is fixed at the beginning of a simulation, meaning this quantity can be pre-computed given a particular phase field.

Romano *et al.* have demonstrated success using the grey phonon formulation including the order parameter function in a 1-dimensional slab test problem [30]. The test problem prescribes the order parameter, illustrated in Figure 8, as a function of position x as

$$\eta(x) = \frac{1}{2} \left(1 + \operatorname{erf} \left(\frac{x - x_0}{\gamma} \right) \right). \tag{60}$$

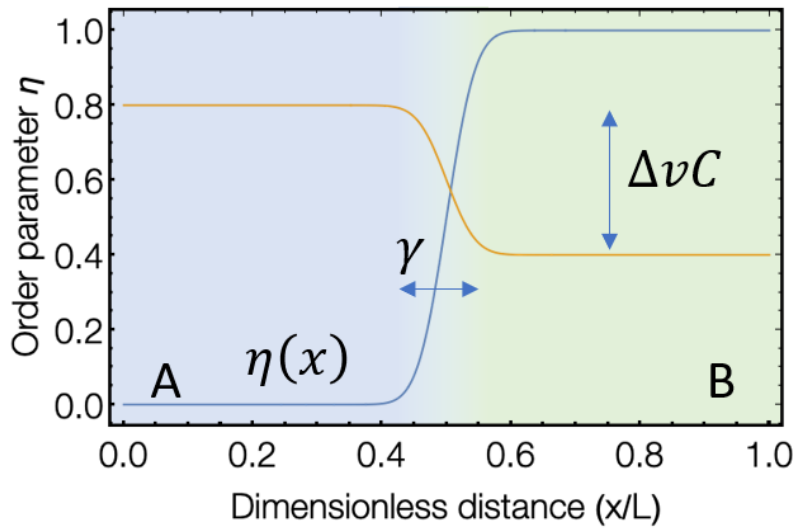

Figure 8: 1D slab order parameter test problem.

Tests in three increasingly complex cases return physical temperature gradients and energy conserving heat flux, as illustrated in Figure 9. The final successful test most importantly demonstrated pairs together two dissimilar materials.

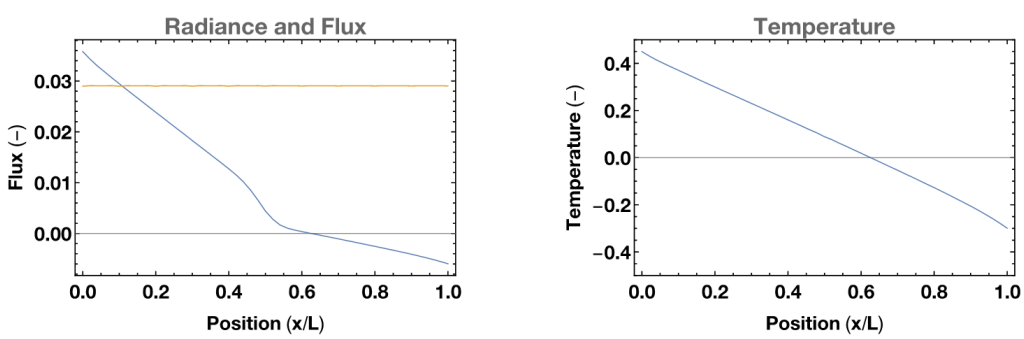

Figure 9: 1D slab order parameter test problem results.

3.3.2 Order parameter method for moving interfacial scattering into the frequency, temperature dependent BTE

A natural extension of the grey formulation is to incorporate the order parameter evaluation into a multi-frequency, temperature dependent formulation as developed in the previous section.

Extending the grey case and using the SAAF formulation, we obtain a frequency and temperature dependent formulation with an order parameter

$$
\begin{aligned}
-\boldsymbol{\Omega}_g \cdot \nabla\Big[\Lambda_g[T^{(\ell)}]\boldsymbol{\Omega}_g \cdot \nabla I_g^{(k+1,\ell)}\Big] + \frac{1}{\Lambda_g[T^{(\ell)}]} I_g^{(k+1,\ell)} = \\
-\boldsymbol{\Omega}_g \cdot \nabla(1+\alpha)\Big[I_g^0[T^{(\ell)}] - \gamma_g[T^{(\ell)}]\Big(\tilde{W}^0[T^{(\ell)}] - \tilde{W}_s[I_g^{(k,\ell)}]\Big)\Big] \\
+ \frac{(1+\alpha)}{\Lambda_g[T^{(\ell)}]}\Big[I_g^0[T^{(\ell)}] - \gamma_g[T^{(\ell)}]\Big(\tilde{W}^0[T^{(\ell)}] - \tilde{W}_s[I_g^{(k,\ell)}]\Big)\Big]
\end{aligned} \tag{61}
$$

where the order parameter informed scattering modification, α, is defined as

$$
\alpha = \frac{\Delta v C}{v C(\eta)} \boldsymbol{\Omega} \cdot \nabla\eta(\boldsymbol{r}). \tag{62}
$$

The physical interpretation of the addition of the order parameter in both the grey and frequency dependent case is that depending on the angle between phonon travel $\boldsymbol{\Omega}$ and gradient of the order parameter $\nabla\eta$, the addition of the order parameter term essentially either increases or decreases the mean free path in that angle.

Algorithm 3 An iterative algorithm for solving frequency and temperature dependent deterministic phonon transport equation in the SAAF form with order parameter correction

while $||\Delta T^{(\ell)}(\mathbf{r})||_\infty > \epsilon_T$ **do**

$\ell = \ell + 1$

while $||\Delta \tilde{W_s}^{(k,\ell)}(\mathbf{r})||_\infty > \epsilon_s$ **do**

$k = k + 1$

for $\mathbf{\Omega}_g$ *in* $\mathbf{\Omega}$ **do**

$$-\mathbf{\Omega}_g \cdot \nabla \Big[\Lambda_g[T^{(\ell)}]\mathbf{\Omega}_g \cdot \nabla I_g^{(k+1,\ell)}\Big] + \frac{1}{\Lambda_g[T^{(\ell)}]} I_g^{(k+1,\ell)} =$$
$$-\mathbf{\Omega}_g \cdot \nabla (1+\alpha)\Big[I_g^0[T^{(\ell)}] - \gamma_g[T^{(\ell)}]\Big(\tilde{W}^0[T^{(\ell)}] - \tilde{W}_s[I_g^{(k,\ell)}]\Big)\Big]$$
$$+\frac{(1+\alpha)}{\Lambda_g[T^{(\ell)}]}\Big[I_g^0[T^{(\ell)}] - \gamma_g[T^{(\ell)}]\Big(\tilde{W}^0[T^{(\ell)}] - \tilde{W}_s[I_g^{(k,\ell)}]\Big)\Big]$$

end

$\tilde{W_s}^{(k+1,\ell)} = \sum_G A_g[T^{(\ell)}]B_g[T^{(\ell)}]I_g^{(k+1,\ell)}$

$\Delta \tilde{W_s}^{(k+1,\ell)} = \tilde{W_s}^{(k+1,\ell)} - \tilde{W_s}^{(k,\ell)}$

end

$\tilde{W_s}^{(\ell+1)} = \tilde{W_s}^{(k+1,\ell)}$

$I^{(\ell+1)} = I^{(k+1,\ell)}$

$T^{(\ell+1)} = T^{(\ell)} + \left(\frac{\partial \tilde{W}^0}{\partial T}|_{T=T^{(\ell)}}\right)^{-1}(\tilde{W}_s^{(\ell+1)} - \tilde{W}^0)$

$\Delta T^{(\ell+1)} = T^{(\ell+1)} - T^{(\ell)}$

end

$\hat{T} = T^{(\ell+1)}$

$\hat{I} = I^{(\ell+1)}$

$\mathbf{q} = \sum_G \mathbf{\Omega}_g \Gamma_g[\hat{T}]B_g[\hat{T}]\hat{I}_g$

$k_x = -\frac{1}{L}\int \frac{\mathbf{q}\cdot\hat{x}}{\nabla\hat{T}\cdot\hat{x}}\, dx$

4 EXPECTED SCHEDULE

4.1 Gantt Chart

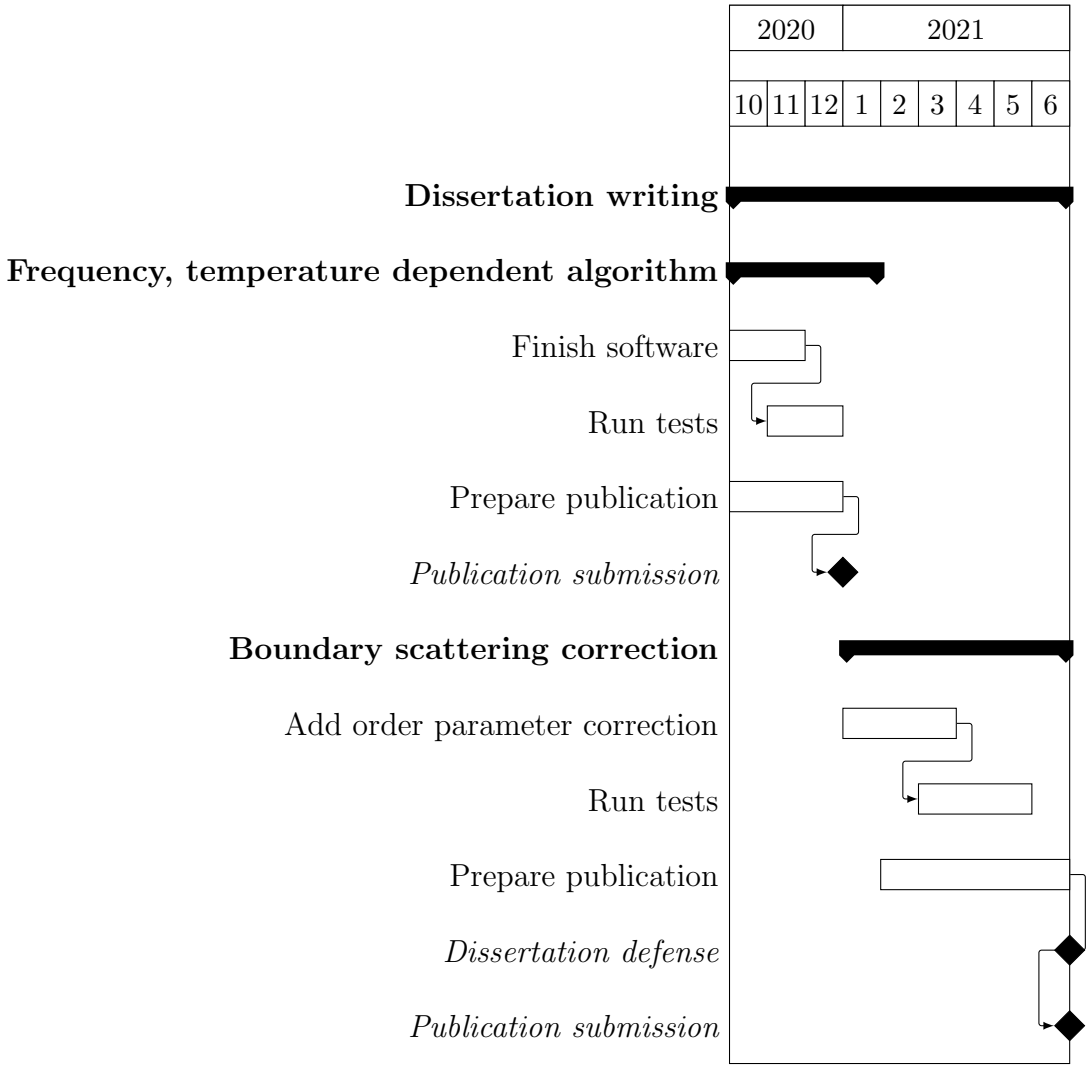

5 TEST PROBLEMS

5.1 Grey phonon transport

This section helps satisfy the objectives outlined in Sec. 2.1.

In order to verify a correct implementation of the methodology, we describe a test problem which uses the Method of Manufactured Solutions (MMS). We also expand on analytical temperature profiles which were calculated by Majumdar, and Yilbas and Bin Mansoor. The temperature profiles used grey phonon data in Silicon. We expand on the grey temperature profiles in silicon and include new grey temperature profile calculations for lithium aluminate. Additionally, we expand on the temperature profile test problems by additionally computing the heat flux, temperature gradient, and thermal conductivity in the grey lithium aluminate test case as a proof of concept.

5.1.1 Method of manufactured solutions spatial convergence study

This study determines the rate of convergence of the outlined method as mesh refinement is increased, and finite element order is increased. This study was adapted from previous work by Woods [22] which used the MFEM finite element library and examined the convergence rate of the spatially first-order form of the Boltzmann neutron transport equation on 2D rectilinear grids with varying finite element order and sinusoidal mesh distortion. The previous work used the DFEM spatial discretization.

We now outline the physical problem in which the MMS study aims to solve. Although phonon annihilation through absorption and internal phonon sources are nonphysical, these computational results may show application in the presence of thermal sinks or generators in the context of refrigeration or heat gen-

eration. Internal angular phonon sources are present in a linearized version of the temperature and frequency dependent discretization of the Boltzmann transport equation for phonons, which will be used in future work. Additionally, since in this Grey formulation the physics are purely scattering — and purely scattering transport problems have no analytical solutions — the use of this MMS problem constitutes a verification of the methodology.

Although in this work the SAAF-SRT-PRT formulation is used, the MMS problem will be described using the SRT-PRT formulation for simplicity. Modifications to the SAAF-SRT-PRT are made as similar to the derivation in Section 3.1.2.

We now make modifications to the steady state SRT-PRT in Eq. 17 by adding an internal isotropic volumetric phonon source, $Q_{internal}$, and absorption as:

$$\boldsymbol{\Omega} \cdot \boldsymbol{\nabla} I + \frac{I}{\Lambda_{total}} = \frac{I^0}{\Lambda_{scattering}} + \frac{Q_{internal}}{4\pi} \tag{63}$$

by relating the mean free paths for scattering and absorption to the total mean free path

$$\frac{1}{\Lambda_{total}} = \frac{1}{\Lambda_{scattering}} + \frac{1}{\Lambda_{absorption}}. \tag{64}$$

The mean free paths were chosen such that:

$$\frac{1}{\Lambda_{total}} = 1.0 \tag{65}$$

$$\frac{1}{\Lambda_{scattering}} = 0.7 \tag{66}$$

$$\frac{1}{\Lambda_{absorption}} = 0.3 \tag{67}$$

In this MMS study, a solution is prescribed for the angular phonon radiance and the respective internal angular phonon source is determined by,

$$\frac{Q_{internal}}{4\pi}, \tag{68}$$

as a function of position. The solution for the internal source is then used as a source term to which we compare our solution of the angular phonon radiance I subscribed by

$$I(x, y, \mu, \eta) = a + b\mu + c\eta + d\cos(4\pi x)\sin(3\pi y) \tag{69}$$

where μ, η are the magnitudes/components of the direction vector $\boldsymbol{\Omega} =< \mu\ \hat{\boldsymbol{x}}, \eta\ \hat{\boldsymbol{y}}, \xi\ \hat{\boldsymbol{z}} >$ in the x and y-directions respectively, and where

$$a = 10 \tag{70}$$

$$b = 1 \tag{71}$$

$$c = 5 \tag{72}$$

$$d = 1. \tag{73}$$

In the original work by Woods [22], the manufactured solution was chosen to be a sinusoidal function such that the solution could not be captured exactly using polynomial basis functions.

Substituting in the manufactured solution from Eq. 69 into Eq. 63, the following solution for the internal source is obtained

$$\frac{Q_{internal}}{4\pi} = a[\frac{1}{\Lambda_{total}} - \frac{1}{\Lambda_{scattering}}] + b[\frac{\mu}{\Lambda_{total}}] + c[\frac{\eta}{\Lambda_{total}}] + d[-4\pi\mu\sin(4\pi x)\sin(3\pi y) + 3\pi\eta\cos(4\pi x)\cos(3\pi y) + \frac{1}{\Lambda_{total}}\cos(4\pi x)\sin(3\pi y) - \frac{1}{\Lambda_{scattering}}\cos(4\pi x)\sin(3\pi y)]. \tag{74}$$

The Dirichlet boundary conditions for this problem are specified on the exterior of the problem domain by substituting either $x = 0$, $y = 0$, $x = 1$, or $y = 1$, in Eq. 69 for the left, bottom, right, and top problem boundaries respectively.

This problem was solved on as base rectilinear grid which spanned 4 x 4 cells with $x \epsilon [0, 1]$ and $y \epsilon [0, 1]$. Where feasible in lower finite element spatial orders, the mesh was refined such that the grid was 8 x 8 and 16 x 16. Finite element orders used were $1, 2, 4$, and 8. The combination of finite element order and grid refinement were chosen such that the number of spatial unknowns matched. The rectilinear grid was also distorted sinusoidally such that the surfaces of the mesh elements were either linearly or quadratically represented, illustrated by Fig. 10.

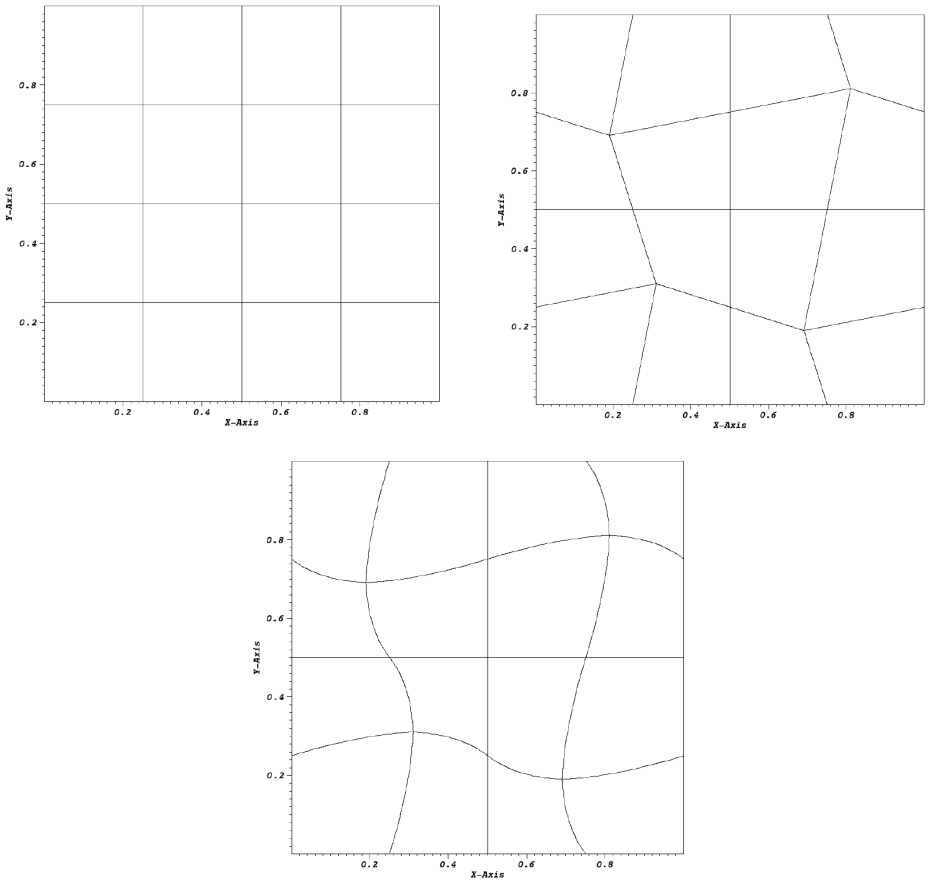

Figure 10: Unrefined orthogonal, linear, and quadratic meshes used in the MMS study.

5.1.2 Temperature calculation in silicon and lithium aluminate

Previous work has calculated the temperature profiles in thin silicon films for various 1D, and 2D configurations [2]. The aim of this research was to examine phonon transport in thin silicon films, primarily for semiconductor applications. The data for this grey phonon transport simulation was documented in previous work by Majumdar [1] and is shown in Table 3. Previous work has also replicated the results of the 1D temperature profile in the fi-

nite element deterministic transport solver named Rattlesnake in the MOOSE computational framework [3].

In a dimensionlessly scaled simulation on the same domain thickness in terms of mean free paths, the temperature profiles obtained should be similar, regardless of actual mean free path magnitudes. Therefore, the expansion of the test cases to include grey phonon data for lithium aluminate should provide similar results as those reported in silicon.

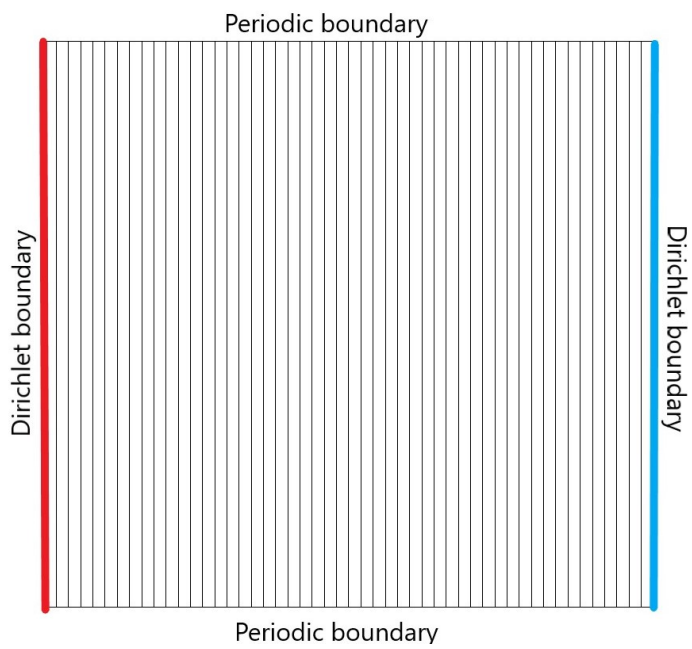

Figure 11: 2D periodic mesh used in temperature profile calculations.

Table 3: Grey silicon phonon data.

Λ (m)	C (J/m^{3}K)	v (m/s)	T$_L$ (K)	T$_R$ (K)
3.38 x 10^{-8}	1.653 x 10^6	8.430 x 10^3	301	300

Table 4: Grey lithium aluminate phonon data.

Λ (m)	C (J/m^{3}K)	v (m/s)	T$_L$ (K)	T$_R$ (K)
1.663 x 10^{-8}	2.636 x 10^6	2.510 x 10^2	301	300

To directly compare to previous work, this temperature calculation utilized a domain thickness of 3Λ and the results were scaled such that the temperature is dimensionless. The dimensionless temperature, Θ, is defined as

$$\Theta = \frac{T(x) - T_L}{T_L - T_R} \tag{75}$$

where T_L and T_R are the hot and cold Dirichlet boundary conditions on temperature, respectively. This results in a temperature scaled from [0, 1] as a function of position x. The distance, or x-axis, was scaled simply from [0, 1] by

$$x \rightarrow \frac{x}{L}, \tag{76}$$

where L is the total domain thickness. In this work, the chosen domain thicknesses are in multiples of the phonon mean free path Λ in m.

5.1.3 Grey thermal conductivity estimate in lithium aluminate

We expand on the previous temperature profile study and incorporate estimates of thermal conductivity in lithium aluminate. In this simulation, we prescribe Dirichlet boundary conditions on temperature T, and thus angular

phonon flux I, on the left and right boundaries as in the previous temperature calculation. For this test case which examines the thermal conductivity profile, we prescribe a domain thickness in the x-direction of 10 Λ, with 50 spatial cells using the same mesh as in Fig. 11.

In these test cases, we also examine the influence of the size of the problem domain on the resulting thermal conductivity profile. In the grey cases, we expect that the kinetic theory approximation of thermal conductivity is appropriate away from boundaries. In these simulations, we model grey lithium aluminate with domain thicknesses of 20Λ and 30Λ keeping the same number of spatial cells.

Previous work simulating frequency dependent phonon transport by Harter *et al.* [28] has shown that adaptive mesh refinement nearest to the boundary as well as increased simulation thickness can decrease the magnitude of boundary effects.

5.2 Temperature and frequency dependent phonon transport

5.2.1 Perfect lithium aluminate

This test helps satisfy the objectives outlined in Sec. 2.

The first test problem is a uniform domain of lithium aluminate with homogeneous temperature boundary conditions at 300 K on each side. The algorithm will first be tested with no temperature interpolation using data constant at 300 K. After that case has been thoroughly tested for proper convergence, we will add in the temperature dependent data interpolation necessary. We anticipate using the same type of spatial mesh as that used in the previous

section.

This test case helps verify the temperature and frequency dependent algorithm has been implemented correctly.

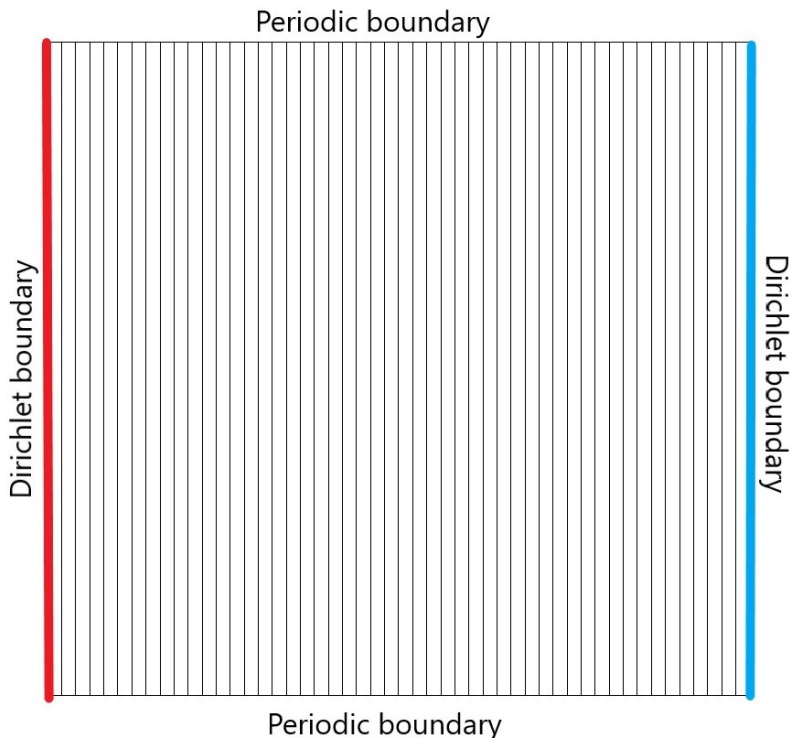

Figure 12: Homogeneous material with isothermal boundary test case.

Once the uniform temperature case has verified a correct implementation of the algorithm, we anticipate that the next step will be modifying the previous test problem to simply reflect a temperature gradient, allowing for a thermal conductivity estimate.

5.3 Order parameter grey and frequency, temperature dependent phonon transport

These test cases help satisfy the objectives outlined in Sec. 2.3.

Grain boundary thermal conductivity between lithium aluminate and lithium pentaluminate will be modeled using the order parameter method. Similar as to previous tests in homogeneous lithium aluminate we will use an induced temperature gradient with hetergeneous materials, as demonstrated in Figure 13. We anticipate both grey cases, and frequency and temperature dependent cases will examine the effect of the domain size on the resulting effective thermal conductivity. Before applying a temperature gradient in the grain boundary thermal conductivity case, a uniform temperature profile will be applied to ensure algorithm performance is as expected, as well as energy conservation.

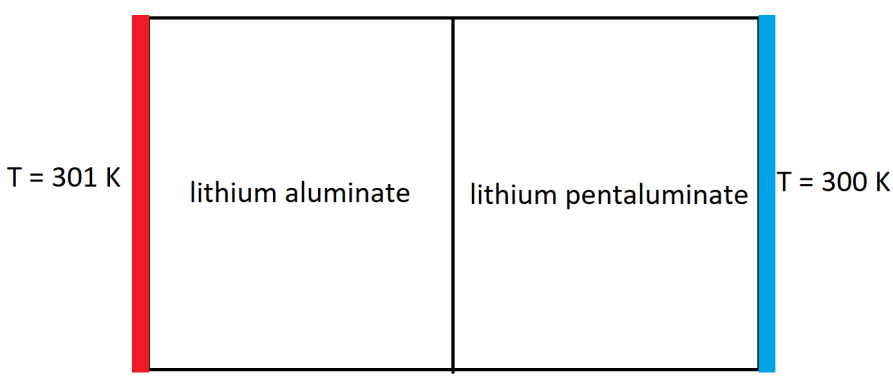

Figure 13: Heterogeneous material with thermal gradient test case.

We will assess the performance of the order parameter method to determine effectiveness.

6 PRELIMINARY RESULTS

6.1 Grey phonon transport

6.1.1 Method of manufactured solutions spatial convergence study

Fig. 14 shows the l_2-norm of the difference between the manufactured solution in Eq. 69 and the solution obtained through the iterative solution with a convergence criterion $\Delta = 10^{-12}$. Each data set is denoted by a finite element order and the order of sinusoidal mesh distortion where applicable.

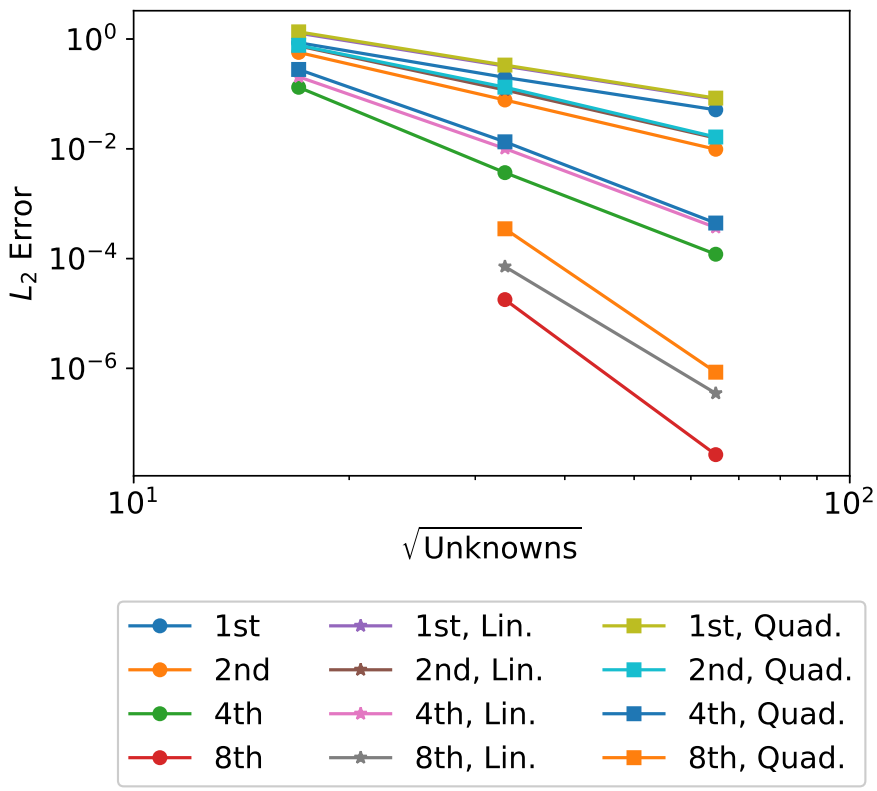

Figure 14: Method of manufactured solutions spatial convergence study.

These results demonstrate that the grey phonon transport algorithm was correctly implemented, and also quantitatively demonstrate that the spatial convergence rates do not suffer greatly when meshes with curved surfaces are used. With a small penalty of initial convergence, the convergence rates using meshes with curved surfaces are the same as for rectilinear meshes. The latter observation agrees with previous work performed by Woods [22].

6.1.2 Temperature calculation in silicon and lithium aluminate

For grey phonon transport calculations that are scaled dimensionlessly, on the same domain thickness in terms of mean free path, the temperature profile obtained should be expected to match as shown in Fig. 15. The results shown in Fig. 15 compare two calculations using our methodology compared to identical previous work by Majumdar [1].

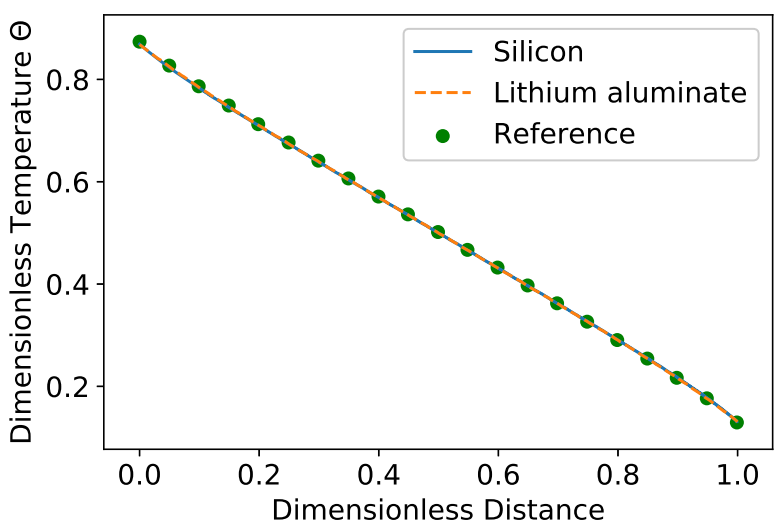

Figure 15: Dimensionless temperature distribution for 3Λ thickness.

The computational results to which we compare our results use the same grey approximation outlined in Sec. 3.1.2, but in a 1D finite difference spatial dicretization scheme rather than finite elements. Previous work by Harter et al. demonstrated similar results using the same approximations and discretization methods used in this work [3].

6.1.3 Grey thermal conductivity estimate in lithium aluminate

Shown in Fig. 16 is the thermal conductivity profile obtained in the grey lithium aluminate test cases for domain thicknesses of 10Λ, 20Λ, and 30Λ. The thermal conductivity rises from a minimum at the problem boundary, which is seen in previous work by Harter et al. Yilbas and Bin Mansoor observed similar boundary effects in their work studying determinstic phonon transport in 1D thin films [2].

As expected from previous studies, the thermal conductivity approaches the kinetic theory approximation, or the diffuse approximation, shown in Eq. 27, in the interior of the domain.

In our experience, we found that for quadrature orders greater than S_2 (equivalent to a diffusion spatial discretization in 1D) caused significant boundary effects. The deviation in the solution from the kinetic theory approximation near the boundaries. The deviation from kinetic theory and Fourier behavior near the boundaries was also observed in the work performed by Harter et al. simulating identical test cases using Grey data for graphite [3].

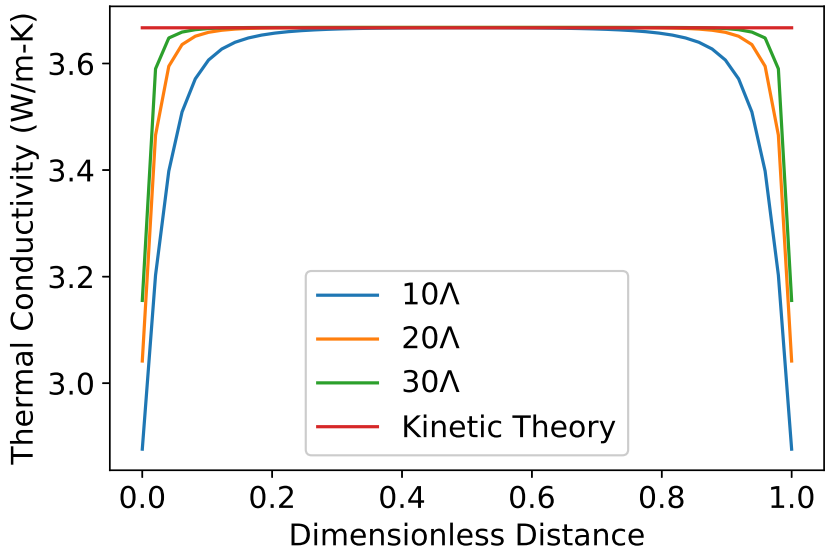

Figure 16: Grey thermal conductivity profiles in lithium aluminate.

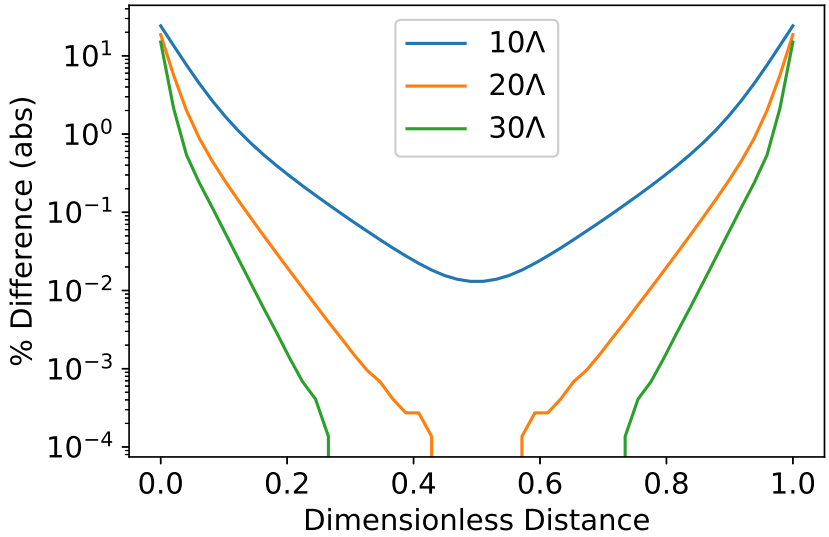

Figure 17: Deviation from kinetic theory, abs. % difference.

In Fig. 17, we note that the simulation using a domain thickness of 30Λ was able to reach the exact kinetic theory estimate in the interior of the domain,

noting that the % difference drops to 0, which can not be seen on the log scale graph.

Additionally, we find that these simulations that compute infinitesimal thermal conductivity in the grey approximation are sensitive to the heat flux calculation. Due to spectral radii very close to 1, the iterations required to resolve the heat flux for larger domains grows computationally demanding.

7 CONCLUDING REMARKS

We present a method for predicting thermal conductivity using deterministic grey phonon transport with the advantages of having the flexibility to use arbitrarily higher-order finite elements, and structured or unstructured meshes with curved surfaces. These features offer computational flexibility for material interfaces which may contain curved features, or for automatic mesh refinement near material interfaces. Our method was verified using a MMS study and demonstrated that convergence rates do not suffer greatly by using meshes with curved surfaces, similar to previous results.

Our results also compare favorably with previous results of phonon transport temperature profiles in 1D thin silicon films, and previous deterministic transport simulations using identical approximations, and spatial and angular discretizations.

We demonstrate that in larger domain thicknesses, the effect of boundaries are mitigated which agrees with the transition from ballistic to diffuse phonon transport as noted by various previous work. However, as shown in previous work by Harter et al., boundary effects are also heavily influenced by the mesh coarseness and can be mitigated through mesh refinement near the boundaries.

Previous work by Harter et al. has taken a slightly different approach when coupling the spectral effects of frequency dependent phonon transport by using a corrective term which changes based on the mismatch between the transport simulations and the expected equilibrium values [28].

Future research will examine temperature and frequency-dependent phonon transport through linearization of the Bose-Einstein phonon emission source in Eq. 9 and a corrective term which links the disparity between the total

phonon scattering term and the total phonon emission term. The linearization and iterative method together resembles a phonon capture and simultaneous re-emission, hence its designation as a pseudo-scattering iteration. Since the method also uses temperature dependent values, temperature must also be iterated upon.

Although the linearization approach is novel in phonon transport simulations, this methodology has previously been applied with success to thermal radiation transport. In future work the frequency, and temperature dependent SAAF-SRT-PRT equation will be linearized, use angularly dependent mean free path data to solve for angular phonon intensities, and use those radiances to determine the thermal properties through discrete summations which are weighted by molecular dynamics simulations.

To handle material heterogeneity and boundary scattering, we plan to use a method which uses a scalar field called the order parameter, which is informed from phase fields. Previous work by Romano et al. has successfully demonstrated applicability of the order parameter method with a grey phonon formulation. Future work will examine a multi-frequency, temperature dependent order parameter method. This method could potentially be applicable in other purely scattering media with complex boundary scattering phenomenon, such as visible light transport.

The grey method has been studied previously and provides a foundation for our proposed work. The multi-frequency algorithm is a new and novel method for performing multi-frequency phonon transport. Additionally, the order parameter method coupled to the multi-frequency and temperature dependent algorithm provides a novel method to account for boundary and interfacial scattering.

8 ACKNOWLEDGEMENTS

The author acknowledges the financial support of Pacific Northwest National Laboratory (PNNL). PNNL is operated by Battelle Memorial Institute for the U.S. Department of Energy under Contract No. DE-AC05-76RL01830. This work was supported by the National Nuclear Security Administration, Tritium Sustainment Program through contract with Oregon State University and University of California-Riverside.

The author also would like to acknowledge their doctoral advisor, committee, collaborators, colleagues at UC-Riverside, PNNL, and Oregon State University, as well as their family and friends for their unwavering support.

References

[1] A. Majumdar. "Microscale Heat Conduction in Dielectric Thin Films". In: *Journal of Heat Transfer* 115.7 (1993), pp. 7–16.

[2] B.S. Yilbas and S. Bin Mansoor. "Frequency dependent phonon transport in two-dimensional silicon and diamond thin films". In: *Modern Physics Letters B* 26.17 (2012).

[3] J. Harter. "Predicting Thermal Conductivity in Nuclear Fuels Using Rattlesnake-Based Deterministic Phonon Transport Simulations". Master's Thesis. Oregon State University, 2015.

[4] J. Charpin et al. "Investigation of γ Lithium Aluminate as Tritium Breeding Material for a Fusion Reactor Blanket". In: *Fusion Engineering and Design* 8 (1989), pp. 407–413.

[5] D. McMorrow. *Tritium*. Technical Report JSR-11-345 - The MITRE Corporation. 2011.

[6] S. Sohinki. "Tritium Readiness Campaign". National Nuclear Security Administration. 2001.

[7] U.S. Department of Energy. *Tritium and Enriched Uranium Management Plan Through 2060*. Report to Congress. 2015.

[8] D.J. Senor. "Commercial Light Water Production of Tritium: Update and Path Forward". Presented at Tritium Focus Group Meeting. 2013.

[9] S. Hu et al. "Assessment of Effective Thermal Conductivity in U–Mo Metallic Fuels". In: *Journal of Nuclear Materials* 462 (2015).

[10] J. Charpin et al. "Investigation of γ lithium aluminate as tritium breeding material for a fusion reactor blanket". In: *Fusion Engineering and Design* 8 (1989), pp. 407–413.

[11] D.J. Senor. "Science and Technology Supporting the Tritium Sustainment Program". Presented at the 40th Tritium Focus Group Meeting, Albuquerque, NM. 2018.

[12] D.E. Burkes et al. "Performance Modeling of TPBAR Pellets". Presented at the Tritium Focus Group, Oak Ridge, TN. 2018.

[13] C. Kittel. *Introduction to Solid State Physics, 8th Ed.* John Wiley & Sons, Inc., 2005.

[14] A.C. Sparavigna. "The Boltzmann Equation Of Phonon Thermal Transport Solved In the Relaxation Time Approximation – I – Theory". In: *Mechanics, Materials Science & Engineering Journal* (Feb. 2016).

[15] D.P. Sellan et al. "Cross Plane Phonon Transport in Thin Films". In: *Journal of Applied Physics* 108 (2010).

[16] J.M. Ziman. *Electrons and Phonons: The Theory of Transport Phenomena in Solids*. Oxford University Press, London, United Kingdom, 1960.

[17] A. Mittal and S. Mazumder. "Monte Carlo Study of Phonon Heat Conduction in Silicon Thin Films Including Contributions of Optical Phonons". In: *Journal of Heat Transfer* 132 (2010).

[18] K.T. Regner et al. "Broadband phonon mean free path contributions to thermal conductivity measured using frequency domain thermoreflectance". In: *Nat. Commun.* 4:1640 (2013).

[19] V.M. Laboure, R.G. McClarren, and Y. Wang. "Globally Conservative, Hybrid Self-Adjoint Angular Flux and Least-Squares Method Compatible with Voids". In: *Nuclear Science and Engineering* 185 (2017), pp. 294–306.

[20] Jim Morel and J M. McGhee. "A Self-Adjoint Angular Flux Equation". In: *Nuclear Science and Engineering* 132 (July 1999), pp. 312–325.

[21] *MFEM: Modular Finite Element Methods Library*. `mfem.org`. DOI: `10.11578/dc.20171025.1248`.

[22] D.N. Woods. "High Order Finite Elements SN Transport in X-Y Geometry on Meshes with Curved Surfaces in the Thick Diffusion Limit". Master's Thesis. Oregon State University, 2016.

[23] D.N. Woods. "Discrete Ordinates Radiation Transport using High-Order Finite Element Spatial Discretizations on Meshes with Curved Surfaces". PhD Dissertation. Oregon State University, 2018.

[24] D.N. Woods and T.S. Palmer. "R-Z Geometry Discrete Ordinates Radiation Transport Using Higher-Order Finite Element Spatial Discretizations on Meshes with Curved Surfaces". In: *Journal of Computational and Theoretical Transport* 48 (2019), pp. 109–128.

[25] Y. Wang, H. Zong, and R.C. Martineau. "Diffusion Acceleration Schemes for Self-Adjoint Angular Flux Formulation with a Void Treatment". In: *Nuclear Science and Engineering* 176 (2014), pp. 201–225.

[26] M.L. Adams and E.W. Larsen. "Fast Iterative Methods for Discrete-Ordinates Particle Transport Calculations". In: *Progress in Nuclear Energy* 40 (2002).

[27] D. Anistratov. "Research Notes - On Iteration Method for Steady-State Boltzmann Transport Problem". Personal Communication. 2019.

[28] J.R. Harter et al. "Prediction of Thermal Conductivity in Dielectrics Using Fast, Spectrally-Resolved Phonon Transport Simulations". In: *International Journal of Heat and Mass Transfer* 144 (2019).

[29] J.R. Harter, T.S. Palmer, and P.A. Greaney. "Predicting Mesoscale Spectral Thermal Conductivity using Advanced Deterministic Phonon Transport Techniques". In: Advances in Heat Transfer. Elsevier, 2020.

[30] G. Romano et al. "Moving Interfacial Scattering Into the Boltzmann Transport Equation for Transport Simulations of Phonons". International Conference on Transport Theory, Paris. 2019.

9 APPENDIX

9.1 Appendix A: 131-group $LiAlO_2$ properties

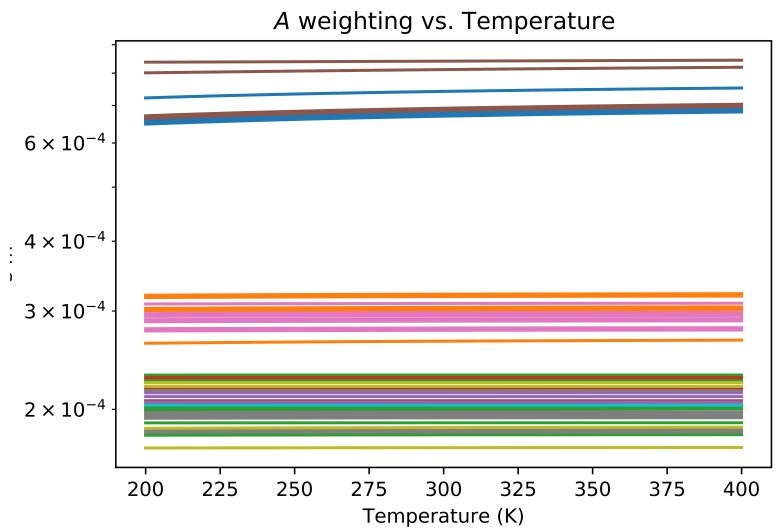

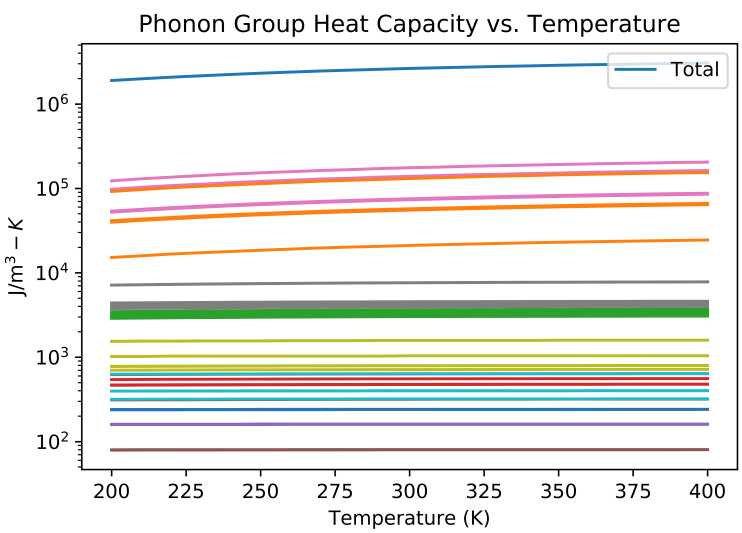

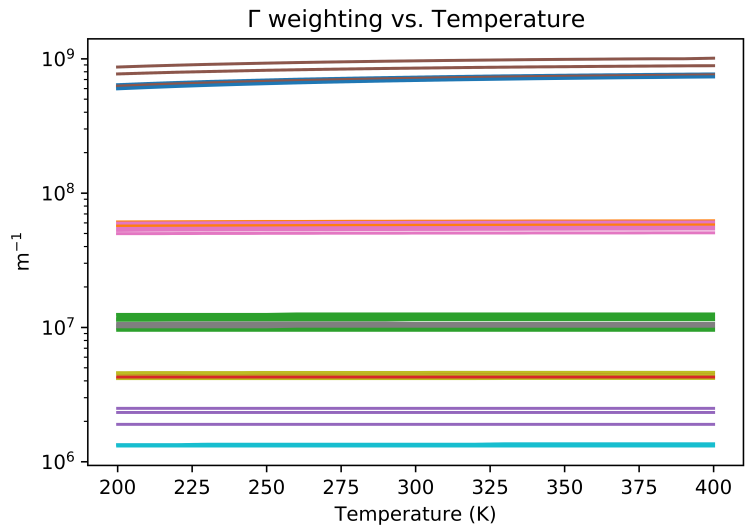
Γ weighting vs. Temperature
10^9
10^8
10^7
10^6
m^{-1}
200
225
250
275
300
325
350
375
400
Temperature (K)

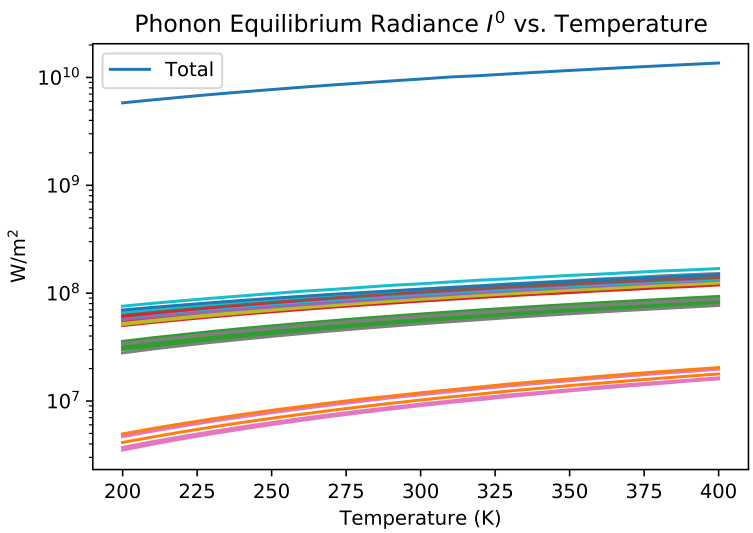
Phonon Equilibrium Radiance I^0 vs. Temperature
Total
10^{10}
10^9
10^8
10^7
W/m^2
200
225
250
275
300
325
350
375
400
Temperature (K)

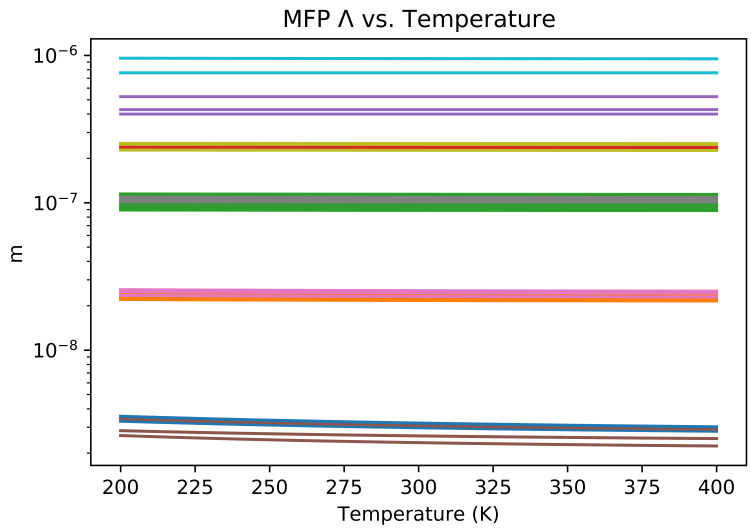
MFP Λ vs. Temperature
10^{-6}
10^{-7}
10^{-8}
m
200
225
250
275
300
325
350
375
400
Temperature (K)

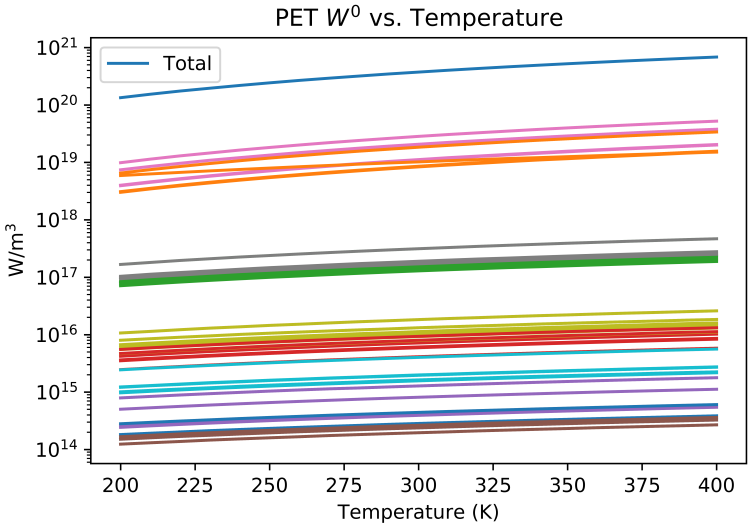
PET W^0 vs. Temperature
Total
10^{21}
10^{20}
10^{19}
10^{18}
10^{17}
10^{16}
10^{15}
10^{14}
W/m^3
200
225
250
275
300
325
350
375
400
Temperature (K)

9.2 Journal Articles and Contributed Summary

Grey Phonon Transport Prediction of Thermal Conductivity in Lithium Aluminate with Higher-Order Finite Elements on Meshes with Curved Surfaces

Nicholas H. Whitman*, **Todd S. Palmer**
School of Nuclear Science and Engineering, Oregon State University, Corvallis, OR 97330

P. Alex Greaney, S. Aria Hosseini
Dept. of Mechanical Engineering, University of California–Riverside, Riverside, CA 92521

Douglas E. Burkes, David J. Senor
Pacific Northwest National Laboratory, Richland, WA 99354

ABSTRACT

We present a method for predicting thermal conductivity by solving the Boltzmann transport equation for grey phonons deterministically by utilizing arbitrary higher-order continuous finite elements on meshes which may also be unstructured and utilize curved surfaces. The self-adjoint angular flux formulation of the grey, steady-state, single relaxation time, phonon radiative transport equation was spatially discretized using the continuous finite element method and angularly discretized using the discrete ordinates (S_N) method. The solution discretization methodology was verified using a method of manufactured solutions spatial convergence test case, and compares favorably to previous work utilizing the discontinuous finite element formulation of the spatially first order form of the radiative transport equation using the same finite element library. The discretized equations were used to solve for the angular phonon radiances, heat flux, and temperature, and was shown to compare favorably to previous literature demonstrating temperature profiles in silicon thin films. Utilizing the local values of the temperature gradient and heat flux, the thermal conductivity as a function of position in a one-dimensional perfect crystal was evaluated using a Fourier's Law representation and compared to a kinetic theory estimate. Our results show that in the interior of the simulation domain, our transport-based prediction of thermal conductivity converges on the kinetic theory estimation. We also find that near isothermal boundaries, the transport solution deviates from kinetic theory implying non-equilibrium behavior in the thin film limit, agreeing with previous studies.

Key Words: phonon transport, radiative transport, discrete ordinates, self-adjoint angular flux, curved surfaces, MFEM

1. INTRODUCTION

1.1 Background and Problem Statement

Prior knowledge of the thermal conductivity of a material is an important parameter required in thermal performance predictions. The physical measurement of a given material's thermal conductivity may be prohibitively expensive and/or difficult, either due to the exotic nature

*Corresponding author. Email: whitmann@oregonstate.edu

of the material or the extreme nature of the environment, a highly radioactive material or environment for example. Therefore, methods which can predict thermal conductivity are highly valuable and less costly to predictive science efforts.

Molecular dynamics, a first principles method, serves as a method for predicting a material's thermal conductivity a priori. These simulations, however, are limited by both simulation size and classical physics.

In larger simulation domain sizes, Boltzmann phonon transport simulations may be more attractive to capture bulk thermal transport behavior, and may more readily couple to multi-physics simulations. Phonon transport predictions of thermal conductivity have historically focused on thin films and dielectrics in semi-conductor applications [1, 2]. Recent research has also shown promise in using deterministic methods of simulating Boltzmann phonon transport to predict thermal conductivity in larger scale ceramic applications, such as uranium dioxide with xenon impurities in nuclear reactor fuels [3].

Lithium aluminate ($LiAlO_2$) is a ceramic material of significant interest to the fusion community, as it is currently one of the most attractive materials for use in neutronic fusion reactors due in part due to its large temperature operating range [4, 5]. Tritium, or ^3H, is a common nuclear fusion fuel and can be produced through neutron absorption reactions in ^6Li and ^7Li. Tritium is also an important asset to the U.S. Department of Energy/National Nuclear Security Administration and must be replenished due its 12.3 year half-life [6, 7].

Lithium aluminate has a micro-structure which changes drastically under neutron irradiation due to the respective density change during precipitations of lithium pentaluminate ($LiAl_5O_8$) which occurs due to lithium depletion. The change in micro-structure during in-reactor irradiation greatly influences heat transport, making time-dependent thermal performance prediction difficult [8]. The goal of this work is to predict thermal conductivity in lithium aluminate as a function of neutron irradiation with deterministic phonon transport simulations which are informed from molecular dynamics data. The thermal conductivity predictions will then serve as inputs to simulations which solve for time and irradiation dependent phase fields, similar to previous methods applied in a uranium-molybdenum system [9].

1.2 Continuum Phonon Transport Physics

In this section, we outline the integral Boltzmann phonon transport equations. We start from the general Boltzmann transport equation for phonons, and outline the assumptions made in this work.

Phonons represent a quantized excitation in the vibrational modes of a solid. Often, phonons are treated as particles rather than waves and as a result are designated as a quasi-particle. The treatment of phonons as quasi-particles allows for individual treatment in Monte Carlo simulations, or bulk treatment in deterministic transport simulations.

We will now outline the governing equations for phonons in this work. The Boltzmann transport

of phonons is governed by Eq. 1

$$\frac{\partial f}{\partial t} + \boldsymbol{v} \cdot \nabla \boldsymbol{f} = \left(\frac{\partial f}{\partial t}\right)_{collision}, \tag{1}$$

where the phonon distribution, $f = f(\boldsymbol{r}, \omega, \boldsymbol{\Omega}, p, t)$, is a function of position ($\boldsymbol{r}$), angular frequency (ω), direction ($\boldsymbol{\Omega}$), polarization (p), and time (t) and where the right-hand side of Eq. 1 describes the rate of change in phonon population due to collision events. The phonon velocity

$$\boldsymbol{v}(\omega, p) = \frac{\partial \omega(\boldsymbol{k}, p)}{\partial \boldsymbol{k}}, \tag{2}$$

is the gradient of ω in wavevector $\boldsymbol{k}$ space obtained through the phonon dispersion relation. The number density of phonons is given by

$$N(\boldsymbol{r}, t) = \sum_p \int_0^{\omega_{max}} d\omega \int_{4\pi} d\boldsymbol{\Omega}\ f(\boldsymbol{r}, \omega, \boldsymbol{\Omega}, p, t) \frac{D(\omega, p)}{4\pi}, \tag{3}$$

where $D(\omega, p)$ is the phonon density of states when spherical symmetry is assumed:

$$D(\omega, p) f(\boldsymbol{r}, \omega, \boldsymbol{\Omega}, p, t) \frac{d\omega d\boldsymbol{\Omega}}{4\pi} = f(\boldsymbol{r}, \boldsymbol{k}, p, t) \frac{d^3\boldsymbol{k}}{(2\pi)^3}. \tag{4}$$

The phonon energy density is defined as

$$E(\boldsymbol{r}, t) = \sum_p \int_0^{\omega_{max}} d\omega \int_{4\pi} d\boldsymbol{\Omega}\ \hbar\omega f(\boldsymbol{r}, \omega, \boldsymbol{\Omega}, p, t) \frac{D(\omega, p)}{4\pi}, \tag{5}$$

and the heat flux is given by

$$\boldsymbol{q}(\boldsymbol{r}, t) = \sum_p \int_0^{\omega_{max}} d\omega \int_{4\pi} d\boldsymbol{\Omega}\ \hbar\omega \boldsymbol{v} f(\boldsymbol{r}, \omega, \boldsymbol{\Omega}, p, t) \frac{D(\omega, p)}{4\pi}. \tag{6}$$

Since energy is conserved in the collision of phonons, the properties of the right hand side of Eq. 1 imply that

$$\sum_p \int_0^{\omega_{max}} d\omega \int_{4\pi} d\boldsymbol{\Omega}\ \hbar\omega \frac{D(\omega, p)}{4\pi} \left(\frac{\partial f}{\partial t}\right)_{collision} = 0. \tag{7}$$

Since the basic phonon properties and governing equations have now been defined, we will now discuss the simplifications and assumptions applied in this work.

The right-hand side of Eq. 1 is commonly simplified by utilizing the single mode relaxation time (SMRT) approximation,

$$\left(\frac{\partial f}{\partial t}\right)_{collision} = \frac{f^0 - f}{\tau}, \tag{8}$$

where $\tau(\omega, p, T)$ is the relaxation time, T is temperature, and where

$$f^0(\omega, T) = n_{BE} = \frac{1}{e^{\frac{\hbar\omega}{k_B T}} - 1}, \tag{9}$$

and n_{BE} is the Bose-Einstein distribution, $\hbar$ is the reduced Plank's constant, and where k_B is Boltzmann's constant [11, 12]. Utilizing the SMRT approximation, Eq. 1 now becomes

$$\frac{\partial f}{\partial t} + \boldsymbol{v} \cdot \boldsymbol{\nabla} f = \frac{f^0 - f}{\tau} \tag{10}$$

The property of the right hand side of Eq. 1 with Eq. 7 leads to

$$\sum_p \int_0^{\omega_{max}} d\omega \int_{4\pi} d\boldsymbol{\Omega}\ \hbar\omega \frac{D(\omega, p)}{4\pi} \left(\frac{f^0 - f}{\tau}\right) = 0, \tag{11}$$

thus leading to the implicit energy balance relationship

$$\sum_p \int_0^{\omega_{max}} d\omega \int_{4\pi} d\boldsymbol{\Omega}\ \hbar\omega \frac{D(\omega, p)}{4\pi} \frac{f^0}{\tau} = \sum_p \int_0^{\omega_{max}} d\omega \int_{4\pi} d\boldsymbol{\Omega}\ \hbar\omega \frac{D(\omega, p)}{4\pi} \frac{f}{\tau}, \tag{12}$$

obtained by rearranging Eq. 11, and is a constraining equation which must be applied in the solution of the equilibrium Boltzmann phonon transport equation.

It is more convenient in the modeling of heat transport to use the term angular phonon radiance which we denote as I, or the intensity of phonons traveling in a given direction $\boldsymbol{\Omega}$. The angular phonon radiance is defined as

$$I(\boldsymbol{r}, \omega, \boldsymbol{\Omega}, p, t) = |\boldsymbol{v}| \hbar\omega D(\omega, p) f(\boldsymbol{r}, \omega, \boldsymbol{\Omega}, p, t) \tag{13}$$

and follows from the Boltzmann transport equation in Eq. 1. The time-dependent phonon radiative transport equation (PRT) following from the SMRT approximation in Eq. 10 is now defined as

$$\frac{1}{v}\frac{\partial I(\boldsymbol{r}, \omega, \Omega, p)}{\partial t} + \boldsymbol{\Omega} \cdot \boldsymbol{\nabla} I(\boldsymbol{r}, \omega, \Omega, p) = \frac{I^0(\omega, p, T) - I(\boldsymbol{r}, \omega, \Omega, p)}{\Lambda(\omega, p, T)}, \tag{14}$$

where the relaxation length, Λ, is defined in terms of the relaxation time and phonon velocity as

$$\Lambda(\omega, p, T) = v\tau(\omega, p, T). \tag{15}$$

The heat flux in Eq. 6, now written in terms of the angular phonon radiance, is now defined as

$$\boldsymbol{q}(\boldsymbol{r}, t) = \frac{1}{4\pi} \int_0^{\omega_{max}} d\omega \int_{4\pi} d\boldsymbol{\Omega}\ \boldsymbol{\Omega} I(\boldsymbol{r}, \omega, \boldsymbol{\Omega}, p, t), \tag{16}$$

or the 1st angular moment of the angular phonon intensity I.

We now assume steady-state in the time-dependent SMRT-PRT equation in Eq. 14 by setting the partial derivative of the angular phonon intensity I with respect to time equal to zero, leading to the steady state, single mode relaxation time, phonon radiative transport equation (SMRT-PRT)

$$\boldsymbol{\Omega} \cdot \boldsymbol{\nabla} I(\boldsymbol{r}, \omega, \Omega, p) + \frac{I(\boldsymbol{r}, \omega, \Omega, p)}{\Lambda(\omega, p, T)} = \frac{I^0(\omega, p, T)}{\Lambda(\omega, p, T)}. \tag{17}$$

1.3 Grey Phonon Transport Approximation

Eq. 17 must still be solved subject to the constraint of energy conservation defined previously in Eq. 12. One approach to achieve this is to assume that phonon collisions only redistribute phonons to different directions, but not to different frequencies. Furthermore, all scattering is treated as elastic, and there is no coupling between the phonon populations at different frequencies. This approximation allows one to model the transport of phonons at each frequency individually as a *grey* population of phonons with the same mean free path and velocity. This so-called multi-grey approach has been shown to be useful for computing thermal conductivity of nano-structures systems with a good trade off between accuracy and efficiency.

In future work, multi-frequency and temperature dependent phonon transport will be considered, but as a step to achieve this, the remainder of this manuscript we restrict our attention to the grey, energy conserving case. Additionally, rather than simulating a series of grey transport groups with different phonon frequncy, we consider a single transport group with an effective mean free path, and phonon radiances obtained from averaging over all of the phonon modes in the modeled materials. This single-group, grey approximation makes for an easy comparison to the kinetic theory approximation for thermal conductivity which will be described later.

For the grey model, we introduce the scalar phonon radiance, ϕ, defined as

$$\phi(\boldsymbol{r}) = \int_{4\pi} d\boldsymbol{\Omega}\ I(\boldsymbol{r}, \boldsymbol{\Omega}) \tag{18}$$

or simply the 0th angular moment of the angular phonon radiance. We similarly define an

equilibrium scalar phonon radiance, ϕ^0, which is a function of system temperature, T, as

$$\phi^0(\boldsymbol{r}, T) = \int_{4\pi} d\boldsymbol{\Omega}\ I^0(\boldsymbol{r}, \boldsymbol{\Omega}, T). \tag{19}$$

We now make an assumption that the angular phonon radiance is isotropic and can be related to the scalar phonon radiance

$$\frac{\phi(\boldsymbol{r})}{4\pi} = I(\boldsymbol{r}, \boldsymbol{\Omega}), \tag{20}$$

which follows from Eq. 18.

The final approximation made is that the equilibrium scalar phonon radiance is equal to the scalar phonon radiance, such that

$$\phi^0 = \phi \tag{21}$$

Under these simplifications and approximations, Eq. 17 is now written as

$$\boldsymbol{\Omega} \cdot \boldsymbol{\nabla} I(\boldsymbol{r}, \boldsymbol{\Omega}) + \frac{I(\boldsymbol{r}, \boldsymbol{\Omega})}{\Lambda} = \frac{I^0(\boldsymbol{r}, \boldsymbol{\Omega})}{\Lambda}. \tag{22}$$

The solution of Eq. 22 through iterative methods will be described in the Methods section.

1.3.1 Heat Transfer Relations

Our assumptions for grey transport thus far have yet to include the relation needed to obtain temperature information from a given equilibrium scalar phonon radiance ϕ^0. The final relation needed to relate the angular phonon radiance, scalar phonon radiance, and temperature is

$$CTv = \phi^0(\boldsymbol{r}, T), \tag{23}$$

where C is the volumetric heat capacity, and v is the phonon group velocity [14]. The product of the volumetric heat capacity and the temperature, CT, can be viewed as the thermal energy density in the system, and v is the velocity at which it is propogating.

By solving for the steady-state scalar-equilibrium phonon radiance, the temperature T is obtained from Eq. 23. The solution for the global temperature, obtained by inverting Eq. 23 for T, can be used to compute the temperature gradient, $\boldsymbol{\nabla} T(\boldsymbol{r})$, which we will use to make a comparison to kinetic theory.

Similar to the method used to compute the scalar phonon radiance in Eq. 18, the heat flux redefined as

$$\boldsymbol{q}(\boldsymbol{r}) = \int_{4\pi} d\boldsymbol{\Omega}\ \boldsymbol{\Omega} I(\boldsymbol{r}, \boldsymbol{\Omega}). \tag{24}$$

In previous phonon transport studies, the thermal conductivity is obtained by computing domain averaged quantities. While Fourier's Law describes the flow of heat averaged over length scales much longer than the phonon mean free path and has little meaning in an infinitesimal limit, it can serve as a useful metric for comparison of the local heat flux and temperature gradient computed from the Boltzmann transport equation. Fourier's Law relates the heat flux, $\boldsymbol{q}(\boldsymbol{r})$, to the temperature gradient $\boldsymbol{\nabla} T(\boldsymbol{r})$ by the thermal conductivity, k as

$$\boldsymbol{q}(\boldsymbol{r}) = -k \boldsymbol{\nabla} T(\boldsymbol{r}), \tag{25}$$

and can be viewed as a diffuse treatment of heat transport. Comparisons against Fourier's Law will determine where diffuse treatment can be expected. In this work, the thermal conductivity reported by using transport calculated values uses an infinitesimal representation of Fourier's Law, rather than using domain averaged quantities.

In anisotropic materials, such as thin films or laminated materials, thermal conductivity is a second rank tensor property. For the problem symmetry that we study here the tensor is diagonal, and its separate components can be obtained from independent simulations in each direction. Periodic boundary conditions on both y-direction boundaries, y = 0 and y = 1 in this case, in a 2-dimensional simulation on the xy-plane allow for an effectively one-dimensional simulation of phonon transport. The handling of the simulation domain and use isothermal boundaries is similar to that used in work by Mittal and Mazumder [13]. The negative quotient of the dot product of both the heat flux and the temperature gradient into the x-direction yield the thermal conductivity in a Fourier's law representation in the x-direction, respectively. This method will be described in greater detail in Section 3.2 by using an illustration in Fig. 2.

$$k_{\boldsymbol{x}} = -\frac{\boldsymbol{q} \cdot \hat{\boldsymbol{x}}}{\boldsymbol{\nabla} T \cdot \hat{\boldsymbol{x}}} \tag{26}$$

As a comparison to the our results of the Boltzmann transport simulation of phonons, we use of the kinetic theory representation of the thermal conductivity defined as

$$k = \frac{\Lambda}{3} C v, \tag{27}$$

which assumes the thermal conductivity is proportional to the mean free path, heat capacity, and velocity of the heat carrier, or phonon in this case [14].

2. METHODOLOGY

2.1 Self-Adjoint Angular Flux Formulation of the SMRT-PRT

In this work, we employ the Self-Adjoint Angular Flux (SAAF) formulation of the phonon radiative transport equation in Eq. 22. The spatially first-order Boltzmann phonon transport equation, Eq. 22, is a hyperbolic equation whereas the SAAF formulation yield a spatially second-order elliptic equation. The SAAF formulation offers several advantages over the spatially first-order radiative transport equation, some of which we will briefly discuss [15]. The SAAF formulation allows for usage of the continuous finite element spatial discretization (CFEM), rather than the discontinuous finite element method (DFEM) which is often used to stabilize the spatially first-order form of the transport equation. CFEM discretizations often result in symmetric positive definite (SPD) matrices, which can be solved with the iterative conjugate gradient (CG) method.

Although there are multiple ways to derive the Self-Adjoint Angular Flux equation, we follow the algebraic derivation outlined previously by Morel and McGhee [16]. We first begin with the steady-state SMRT-PRT equation in Eq. 17. The angular phonon radiance, I, is now written in terms of the streaming operator, $\Lambda\boldsymbol{\Omega}\cdot\boldsymbol{\nabla}I$, and the angular equilibrium phonon radiance, I^0, as

$$I = I^0 - \Lambda\boldsymbol{\Omega}\cdot\boldsymbol{\nabla}I. \tag{28}$$

The expression for the angular phonon radiance, I, is then substituted back into the streaming operator, $\Lambda\boldsymbol{\Omega}\cdot\boldsymbol{\nabla}I$, in Eq. 17. Dividing through by Λ then yields the SAAF-SMRT-PRT equation

$$-\boldsymbol{\Omega}\cdot\boldsymbol{\nabla}(\Lambda\boldsymbol{\Omega}\cdot\boldsymbol{\nabla}I) + \frac{I}{\Lambda} = \frac{I^0}{\Lambda} - \boldsymbol{\Omega}\cdot\boldsymbol{\nabla}I^0. \tag{29}$$

2.2 Discrete Ordinates (S_N) Angular Discretization

In this work, the angular variable is discretized using the discrete ordinates (S_N) method, which subdivides the 4π solid angle unit sphere into a set of discrete angular vectors $[\boldsymbol{\Omega}_1, .., \boldsymbol{\Omega}_N]$ and associated weights $[w_1, .., w_N]$ called the quadrature set, where N is the quadrature order. In this work, the S_8 Level-Symmetric (LQ_8) quadrature set is used.

We omit discussion of the advantages and disadvantages of quadrature selection outside of mentioning that certain quadrature sets are more attractive depending on the the unique problem selection. In general, the choice of quadrature and angular expansion order in the Grey transport of phonons due to the purely scattering nature of phonon physics, as purely scattering media is less prone to ray effects.

In terms of the grey approximation, the continuous angular integrals can now be written as single discrete summation over the ordinates. Using this method, we assume that the scalar phonon radiance $\phi(\boldsymbol{r})$, for example, can be reconstructed by a discrete summation multiplying

the angular phonon radiance $I_n(\boldsymbol{r}, \Omega_n)$ in each angular ordinate by its respective weight w_n

$$\phi(\boldsymbol{r}) = \int_{4\pi} d\boldsymbol{\Omega}\ I(\boldsymbol{r}, \boldsymbol{\Omega}) \longrightarrow \sum_N I_n(\boldsymbol{r}, \boldsymbol{\Omega}_n) w_n(\boldsymbol{\Omega}_n). \tag{30}$$

The discrete heat flux calculation is similar to that as in Eq. 30 but with the inclusion of the direction vector $\boldsymbol{\Omega}$. For example, the heat flux in the x-direction is simply:

$$\boldsymbol{q}_x(\boldsymbol{r}) = \int_{4\pi} d\boldsymbol{\Omega}\ |\boldsymbol{\Omega} \cdot \boldsymbol{x}| I(\boldsymbol{r}, \boldsymbol{\Omega}) \longrightarrow \sum_N \mu_n(\boldsymbol{\Omega}_n) I_n(\boldsymbol{r}, \boldsymbol{\Omega}_n) w_n(\boldsymbol{\Omega}_n), \tag{31}$$

where $\mu_n(\boldsymbol{\Omega}_n)$ is the cosine of the direction vector $\boldsymbol{\Omega}$ with respect to $\hat{x}$.

2.3 Finite Element Spatial Discretization

In this work, we spatially discretize the SAAF-SMRT-PRT in Eq. 29 using the finite element method through the MFEM software package. MFEM is a scalable and modular finite element library written in `C++` and offers the ability to use arbitrarily higher-order finite elements on unstructured meshes with or without curved surfaces [17]. Previous work by Woods has successfully demonstrated the solution of the spatially first-order form of the neutron transport in MFEM, analogous to the SMRT-PRT phonon transport equation in Eq. 22, using discontinuous finite elements (DFEM) using higher-order finite elements on meshes with curved surfaces [19–21]. In this work, however, the continuous finite element discretization (CFEM) is used to spatially discretize the SAAF-SMRT-PRT equation.

Following the derivation of the CFEM finite element formulation for the SAAF neutron transport equation in previous work by Wang, Zong, and Martineau, the SAAF-SMRT-PRT is now written in the weak form using similar notation for volume and surface integrals [22], omitting the reflection terms, as

$$\begin{aligned}(\boldsymbol{\Omega} \cdot \boldsymbol{\nabla} I^*, \Lambda \boldsymbol{\Omega} \cdot \boldsymbol{\nabla} I)_D + (I^*, \frac{I}{\Lambda})_D + \ < I^*, I >_{\delta D^+} = \\ (I^* + \Lambda \boldsymbol{\Omega} \cdot \boldsymbol{\nabla} I^*, I^0)_D + < I^*, I_{inc} >_{\delta D^-}\ .\end{aligned} \tag{32}$$

In Eq. 32, I^* represents the basis function and I represents the test function. The notation for the inner products over the domain D are

$$(I^*, I)_D \ = \int_D I^*(\boldsymbol{\Omega}, \boldsymbol{r}) I(\boldsymbol{\Omega}, \boldsymbol{r})\ d\boldsymbol{r}, \tag{33}$$

and the notation for inner products over the domain surface δD are

$$< I^*, I >_{\delta D} \ = \int_{\delta D} |\boldsymbol{\Omega} \cdot \hat{\boldsymbol{n}}| I^*(\boldsymbol{\Omega}, \boldsymbol{r}) I(\boldsymbol{\Omega}, \boldsymbol{r})\ d\boldsymbol{S}. \tag{34}$$

The inner products over the surface of the domain in Eq. 32 are split into two separate inner products which include either a negative or positive superscript on δD and denote whether the term is for inflow or outflow boundaries respectively. Inflow boundaries are specified on the condition $\boldsymbol{\Omega} \cdot \hat{\boldsymbol{n}} < 0$ and constitute the implementation of the Dirichlet boundary conditions using Eq. 23 to define the incident angular phonon radiance

$$I_{inc} = \frac{CvT(\boldsymbol{r}_b)}{4\pi}, \tag{35}$$

where $T(\boldsymbol{r}_b)$ is the boundary temperature. Additionally, the outflow boundaries are specified by the condition $\boldsymbol{\Omega} \cdot \hat{\boldsymbol{n}} \geq 0$. The inflow boundary condition — which is typically the only condition required in the spatially first-order discretization — *and* the outflow boundary condition are both required for closure in the SAAF spatial discretization. Since the outflow inner product is unknown, it appears on the left hand side of Eq. 32. In the CFEM formulation interior neighbor surfaces are canceled, thus the outflow condition will only appear on the boundary of the entire domain. These phonon transport problems can be classified as purely scattering and boundary driven.

Each term in the weak form of the SAAF-SMRT-PRT in Eq. 32 besides a custom term was implemented by the following standard MFEM bilinear or linear terms in the base library in Table I.

Table I: MFEM bilinear and linear forms.

Weak Form	Integrator Form	Integrator Type	MFEM Form Name
$(\boldsymbol{\Omega} \cdot \boldsymbol{\nabla} I^*, \Lambda \boldsymbol{\Omega} \cdot \boldsymbol{\nabla} I)_D$	Bilinear	Domain	**DiffusionIntegrator**
$(I^*, \frac{I}{\Lambda})_D$	Bilinear	Domain	**MassIntegrator**
$< I^*, I >_{\delta D^+}$	Bilinear	Surface	**DGTraceIntegrator**
$(I^*, I^0)_D$	Linear	Domain	**DomainLFIntegrator**
$(\Lambda \boldsymbol{\Omega} \cdot \boldsymbol{\nabla} I^*, I^0)_D$	Linear	Domain	***Custom**
$< I^*, I_{inc} >_{\delta D^-}$	Linear	Surface	**BoundaryFlowIntegrator**

2.4 Iterative Solution Methodology

We use the standard source iteration technique for numerically solving the SAAF-SMRT-PRT equation [23]. We assume an initial distribution for the scalar phonon radiance ϕ, and solve

for an updated ϕ which is then used on the next iteration, or lagged. This iterative solution methodology is outlined in Algorithm 1.

The spectral radius ρ, which is bounded between 0 and 1, is a measure of how quickly the maximum difference between iterates decreases and is related to the largest eigenvalue of the iteration matrix. In the context of our iterative methodology, the spectral radius is defined in terms of the l_∞ norm of the differences between scalar phonon radiances between iterates, l, as

$$\rho^{(l)} = \frac{|\phi^{(l+1)} - \phi^{(l)}|_\infty}{|\phi^{(l)} - \phi^{(l-1)}|_\infty}. \tag{36}$$

An implication of the iterative solution methodology is that to reach a tolerance ϵ, the number of iterates n required will at least be such that $\rho^n < \epsilon$. The source iteration continues until the differences between the estimates of the scalar phonon radiance, ϕ, are less than some predefined tolerance. For convenience, we define the l_∞ norm of the difference of the scalar phonon radiance estimates as

$$\Delta^{(l)} = |\phi^{(l+1)} - \phi^{(l)}|_\infty, \tag{37}$$

Our convergence criterion is defined as met when the following holds true:

$$\Delta^{(l)} < \epsilon \times (1 - \rho^{(l)}) \times |\phi^{(l)}|_\infty. \tag{38}$$

Algorithm 1: Grey Phonon Transport Source Iteration

Guess $\phi^{0(0)}, I^{0(0)}$
Tolerance $\epsilon = 10^{-8}$
Iterate count $l = 0$
while $\Delta^{(l)} > \epsilon \times (1 - \rho^{(l)}) \times |\phi^{(l)}|_\infty$ **do**
  for $\boldsymbol{\Omega}_n$ *in* $\boldsymbol{\Omega}$ **do**
    $-\boldsymbol{\Omega}_n \cdot \boldsymbol{\nabla}[\Lambda \boldsymbol{\Omega}_n \cdot \boldsymbol{\nabla} I^{(l+1)}] + \frac{I^{(l+1)}}{\Lambda} = -\boldsymbol{\Omega}_n \cdot \boldsymbol{\nabla} I^{0,(l)} + \frac{I^{0,(l)}}{\Lambda}$
  end
  $\phi^{(l+1)} = \sum_N w_n I_n^{(l+1)}$
  $I^{0,(l+1)} = \frac{1}{4\pi}\phi^{(l+1)}$
  $\rho^{(l)} = \frac{|\phi^{(l+1)} - \phi^{(l)}|_\infty}{|\phi^{(l)} - \phi^{(l-1)}|_\infty}$
  $\Delta^{(l)} = |\phi^{(l+1)} - \phi^{(l)}|_\infty$
  $l = l + 1$
end
$\boldsymbol{q} = \sum_N \boldsymbol{\Omega_n} I_n^{(l)} w_n$
$T = \frac{\phi^{(l)}}{Cv}$
$k_x = \frac{-\boldsymbol{q_x}}{\boldsymbol{\nabla T_x}}$

3. TEST PROBLEMS

In order to verify a correct implementation of the methodology, we describe a test problem which uses the Method of Manufactured Solutions (MMS). We also expand on analytical temperature profiles which were calculated by Majumdar, and Yilbas and Bin Mansoor. The temperature profiles used grey phonon data in Silicon. We expand on the grey temperature profiles in silicon and include new grey temperature profile calculations for lithium aluminate. Additionally, we expand on the temperature profile test problems by additionally computing the heat flux, temperature gradient, and thermal conductivity in the grey lithium aluminate test case as a proof of concept.

3.1 Method of Manufactured Solutions Spatial Convergence Study

This study determines the rate of convergence of the solution method as mesh refinement and finite element order is increased. We also examine how using distorted meshes affects the convergence rate. This study was adapted from previous work by Woods which used the MFEM finite element library and examined the convergence rate of the spatially first-order form of the Boltzmann neutron transport equation on 2D rectilinear grids with varying finite element order and sinusoidal mesh distortion [19]. The previous work used the DFEM spatial discretization, however.

We now outline the physical problem in which the MMS study aims to solve. Although phonon annihilation through absorption and the addition of internal phonon sources are nonphysical in the sense of the current grey formulation, these computational results may show application in the presence of thermal sinks or generators in the context of refrigeration or heat generation. Additionally, since in this grey formulation the physics are purely scattering — and purely scattering transport problems have no analytical solutions — the use of this MMS problem constitutes a verification of the method.

Although this work uses the SAAF-SMRT-PRT formulation, this MMS problem will be described using the SMRT-PRT formulation for simplicity. Modifications to the SAAF-SMRT-PRT are made as similar to the derivation in Section 1.3.

We now make nonphysical modifications to the steady state SMRT-PRT in Eq. 17 by adding an internal isotropic volumetric phonon source, $Q_{internal}$, and absorption as:

$$\boldsymbol{\Omega} \cdot \boldsymbol{\nabla} I + \frac{I}{\Lambda_{total}} = \frac{I^0}{\Lambda_{scattering}} + \frac{Q_{internal}}{4\pi} \tag{39}$$

by relating the mean free paths for scattering and absorption to the total mean free path

$$\frac{1}{\Lambda_{scattering}} + \frac{1}{\Lambda_{absorption}} = \frac{1}{\Lambda_{total}} \tag{40}$$

which we chose to be 0.7, 0.3, and 1.0 respectively.

In this MMS study, we prescribe a solution for the angular phonon radiance and determine the respective internal angular phonon source,

$$\frac{Q_{internal}}{4\pi}, \tag{41}$$

as a function of position. The solution for the internal source is then be used as a source term to which we compare our solution of the angular phonon radiance I prescribed by

$$I(x, y, \mu, \eta) = a + b\mu + c\eta + d\cos(4\pi x)\sin(3\pi y) \tag{42}$$

where μ, η are the components of the direction vector $\mathbf{\Omega} =< \mu\ \hat{\boldsymbol{x}}, \eta\ \hat{\boldsymbol{y}}, \xi\ \hat{\boldsymbol{z}} >$ in the x and y-directions respectively, and where

$$a = 10 \tag{43}$$
$$b = 1 \tag{44}$$
$$c = 5 \tag{45}$$
$$d = 1. \tag{46}$$

In the original work by Woods, the manufactured solution was chosen to be a sinusoidal function such that the solution could not be captured exactly using polynomial basis functions.

Substituting the manufactured solution from Eq. 42 into Eq. 39, the following solution for the internal source is obtained

$$\begin{aligned}\frac{Q_{internal}}{4\pi} = a[\frac{1}{\Lambda_{total}} - \frac{1}{\Lambda_{scattering}}] + b[\frac{\mu}{\Lambda_{total}}] + c[\frac{\eta}{\Lambda_{total}}] + d[-4\pi\mu\sin(4\pi x)\sin(3\pi y) + \\ 3\pi\eta\cos(4\pi x)\cos(3\pi y) + \frac{1}{\Lambda_{total}}\cos(4\pi x)\sin(3\pi y) - \frac{1}{\Lambda_{scattering}}\cos(4\pi x)\sin(3\pi y)].\end{aligned} \tag{47}$$

The Dirichlet boundary conditions for this problem are specified on the exterior of the problem domain by substituting either $x = 0$, $y = 0$, $x = 1$, or $y = 1$, in Eq. 42 for the left, bottom, right, and top problem boundaries respectively.

This problem was solved on a base rectilinear grid spanning 4 x 4 cells with $x \epsilon [0, 1]$ and $y \epsilon [0, 1]$. Where feasible in lower finite element spatial orders, the mesh was refined such that the grid was 8 x 8 and 16 x 16. Finite element orders used were $1, 2, 4$, and 8. The combination of finite element order and grid refinement were chosen such that the number of spatial unknowns matched. The rectilinear grid was also distorted sinusoidally such that the surfaces of the mesh elements were either linearly or quadratically represented, illustrated by Fig. 1.

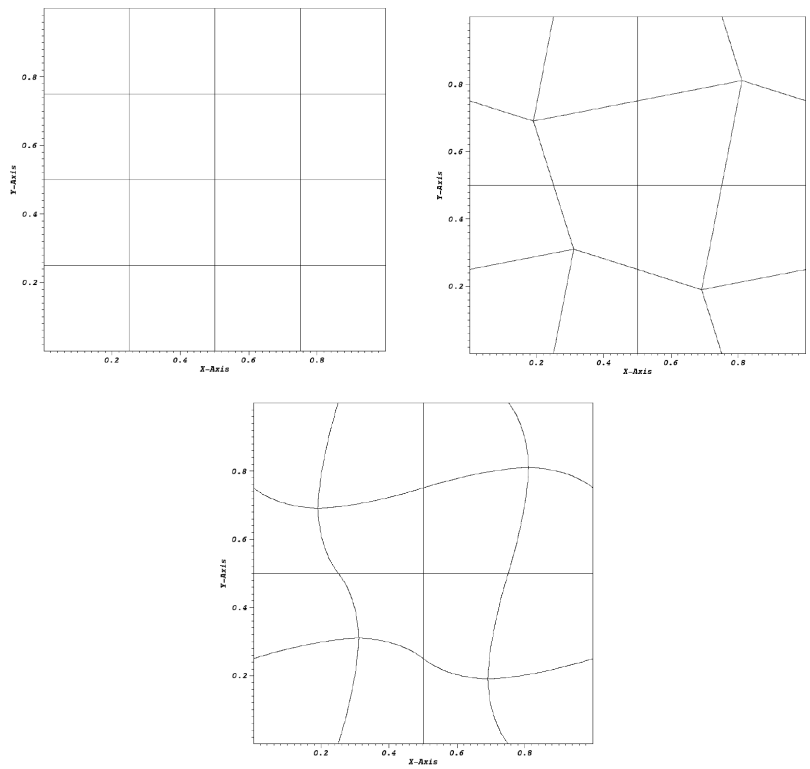

Figure 1: Unrefined orthogonal, linear, and quadratic meshes used in MMS study.

3.2 Temperature Calculation in Silicon, Lithium Aluminate

Previous work has calculated the temperature profiles and effective thermal conductivity in thin silicon films for various 1D, and 2D configurations [2]. The aim of the previous research was to examine phonon transport in thin silicon films, primarily for semiconductor applications. The data for this gray phonon transport simulation was documented in previous work by Majumdar and is shown in Table II [1]. Previous work has also replicated the results of the 1D temperature profile in the finite element deterministic transport solver named Rattlesnake in the MOOSE computational framework [24].

These prior models for silicon provide a test system for validation for our transport model. Going beyond that our goal is to model phonon transport in γ-$LiAlO_2$. This has a tetragonal crystal structure and as a result it's intrinsic thermal conductivity is not isotropic, being between 10% and 15% larger along the c-axis than it is in the basal plane.

The phonon transport properties of $LiAlO_2$ were obtained by computing from first principles the frequency, group velocity and intrinsic three-phonon scattering lifetime for phonon polarizations and numerically integrating the contribution to thermal conductivity from all phonon modes in the Brillouin zone.

Second and third order force constants were computed using density functional theory, and the with the phonon lifetimes from computed the third order force constants using *almaBTE* with a $40 \times 40 \times 40$ k-point Brillouin zone mesh [18].

For the purposes of testing our simulation approach, we average the phonon transport properties in all directions to obtain the effective properties of a single isotropic transport group. The group velocity of this group, shown in Table II), is considerably lower than the speed of the acoustic phonons as it is the average velocity of all phonon modes weighted by their contribution to the phonon radiance, $\omega\hbar f^0(\omega, T)$, with $T = 300$ K. Similarly, the average mean free path is the average of the mean free path of each phonon modes weighted by $\omega\hbar |v_g| f^0(\omega, T)$.

In a dimensionlessly scaled simulation using the same domain thickness in terms of mean free paths, the temperature profiles obtained should be identical, regardless of actual mean free path magnitudes. Therefore, the expansion of the test cases to include grey phonon data for lithium aluminate should provide similar results as those reported in silicon.

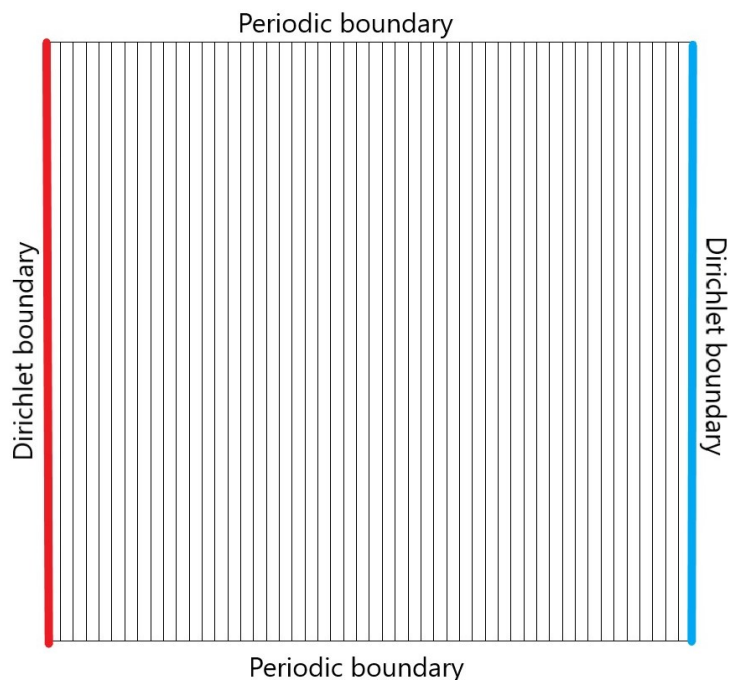

Figure 2: 2D periodic mesh used in temperature profile calculations.

Table II: Grey phonon transport data for Si and $LiAlO_2$.

Material	Λ (m)	C (J/m^{3}K)	v (m/s)	$\kappa_{\text{kin}} = \frac{1}{3}\Lambda C v$ (W/m K)
Si	3.380×10^{-8}	1.653×10^6	8.430×10^3	157.0
$LiAlO_2$	1.663×10^{-8}	2.636×10^6	2.510×10^2	3.668

To directly compare to previous work, this temperature calculation utilized a domain thickness of 3Λ and the results were scaled such that the temperature is dimensionless. The dimensionless

temperature, Θ, is defined as

$$\Theta = \frac{T(x) - T_L}{T_L - T_R} \tag{48}$$

where T_L and T_R are the hot and cold Dirichlet boundary conditions on temperature, respectively. This results in a temperature scaled from [0, 1] as a function of position x. The distance, or x-axis, was scaled simply from [0, 1] by dividing by the domain thickness L

$$x \to \frac{x}{L}. \tag{49}$$

In this work, the chosen domain thicknesses are in multiples of the phonon mean free path Λ in m.

3.3 Thermal Conductivity Estimate in Lithium Aluminate

We expand on the previous temperature profile study and incorporate estimates of thermal conductivity in lithium aluminate. We expand on the previous temperature profile study and incorporate estimates of thermal conductivity in lithium aluminate, using the transport properties in Table II. These In this simulation, we prescribe Dirichlet boundary conditions on temperature T, and thus angular phonon flux I, on the left and right boundaries as in the previous temperature calculation. For this test case examining the thermal conductivity profile, we prescribe a domain thickness in the x-direction of 10 Λ, with 50 spatial cells using the same mesh as in Fig. 2. We also examine the influence of the size of the problem domain on the resulting thermal conductivity profile. In grey cases, we expect that the kinetic theory approximation of thermal conductivity is appropriate away from boundaries where diffuse behavior is applicable. In these simulations, we model grey lithium aluminate with domain thicknesses of 20Λ and 30Λ with the same number of spatial cells.

Previous work by Harter et al. examining frequency dependent phonon transport has shown that mesh refinement as well as increased simulation thickness can decrease the magnitude of boundary effects [26].

4. RESULTS

4.1 Method of Manufactured Solutions Spatial Convergence Study

Fig. 3 shows the l_2-norm of the difference between the manufactured solution in Eq. 42 and the solution obtained through the iterative solution with a convergence criterion $\Delta = 10^{-12}$. Each data set is denoted by a finite element order and the order of sinusoidal mesh distortion where applicable.

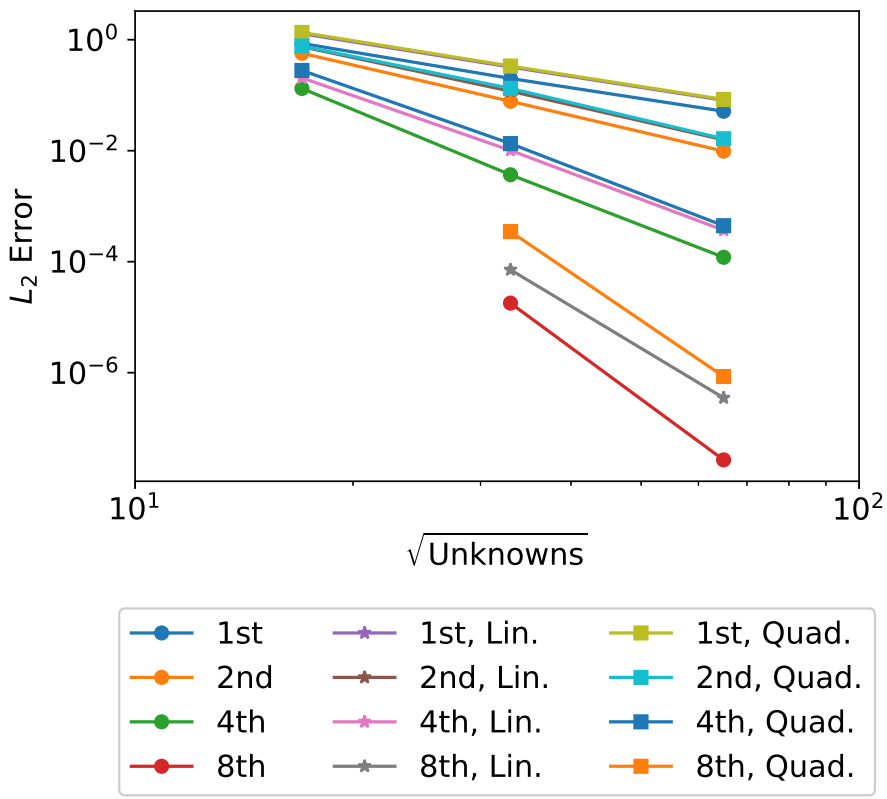

Figure 3: Method of manufactured solutions spatial convergence study.

These results demonstrate that the grey phonon transport algorithm was correctly implemented, and also quantitatively demonstrate that the spatial convergence rates do not suffer greatly when meshes with curved surfaces are used in this test case. With a small penalty of initial convergence, the convergence rates using meshes with curved surfaces are the same as for rectilinear meshes. The latter observation agrees with previous work performed by Woods [19]. Additionally, using higher finite element orders are expected to increase convergence rate, as expected.

4.2 Temperature Calculation in Silicon, Lithium Aluminate

As previously mentioned, grey phonon transport calculations dimensionless scaled on the same domain thickness in terms of mean free path as shown in Fig. 4, the temperature profile obtained should be expected to match identically to previous work by Majumdar [1]. Shown below, our results match with the reference solution. In Fig. 4, the data for silicon and for lithium aluminate overlap as expected.

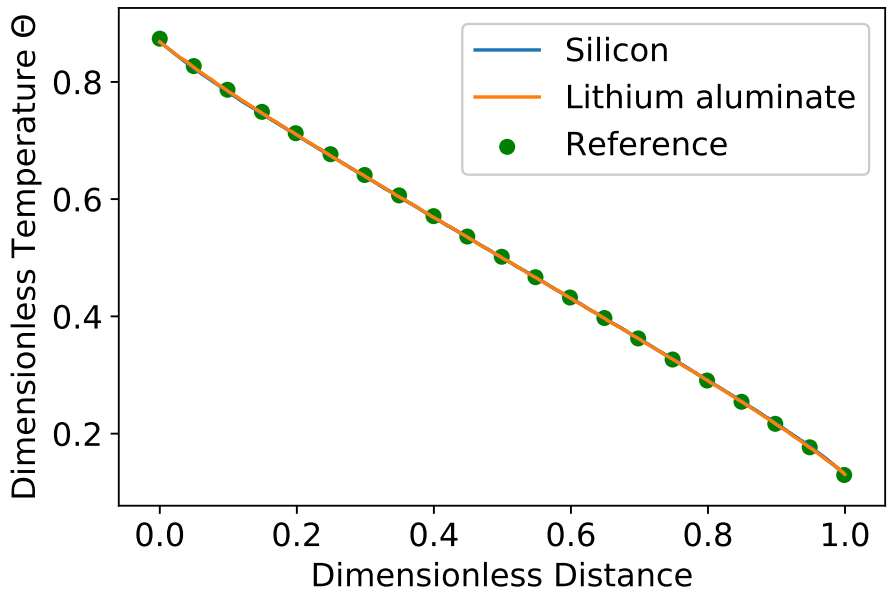

Figure 4: Dimensionless temperature distribution for 3Λ thickness.

The computational results to which we compare our results use the same grey approximation outlined in Sec. 1.3, but in a 1D finite difference spatial dicretization scheme rather than finite elements. Previous work by Harter et al. demonstrated similar results using the same approximations and discretization methods used in this work [24].

4.3 Thermal Conductivity Estimate in Lithium Aluminate

Shown in Fig. 5 is the thermal conductivity profile obtained in the grey lithium aluminate test cases for domain thicknesses of 10Λ, 20Λ, and 30Λ. The thermal conductivity rises from a minimum at the isothermal boundary, which is seen in previous work by Harter et al. Yilbas and Bin Mansoor observed similar boundary effects in their work studying determinstic phonon transport in 1D thin films [2].

As expected from previous studies, the thermal conductivity approaches the kinetic theory approximation, or a diffuse approximation, shown in Eq. 27, in the interior of the domain. The deviation from kinetic theory and Fourier behavior near the boundaries was also observed in the work performed by Harter et al. simulating identical test cases using grey data for graphite [24].

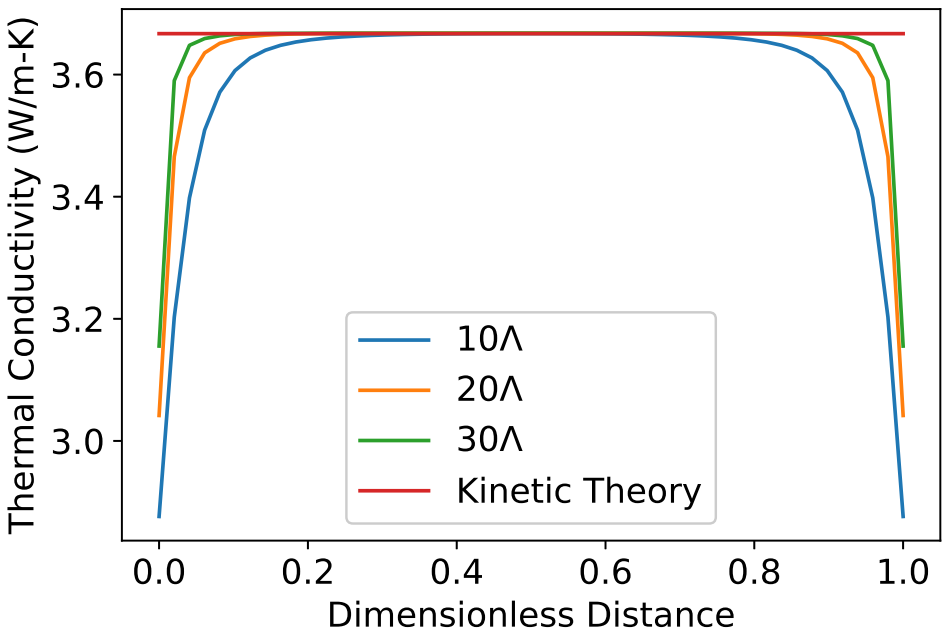

Figure 5: Grey thermal conductivity profiles in lithium aluminate.

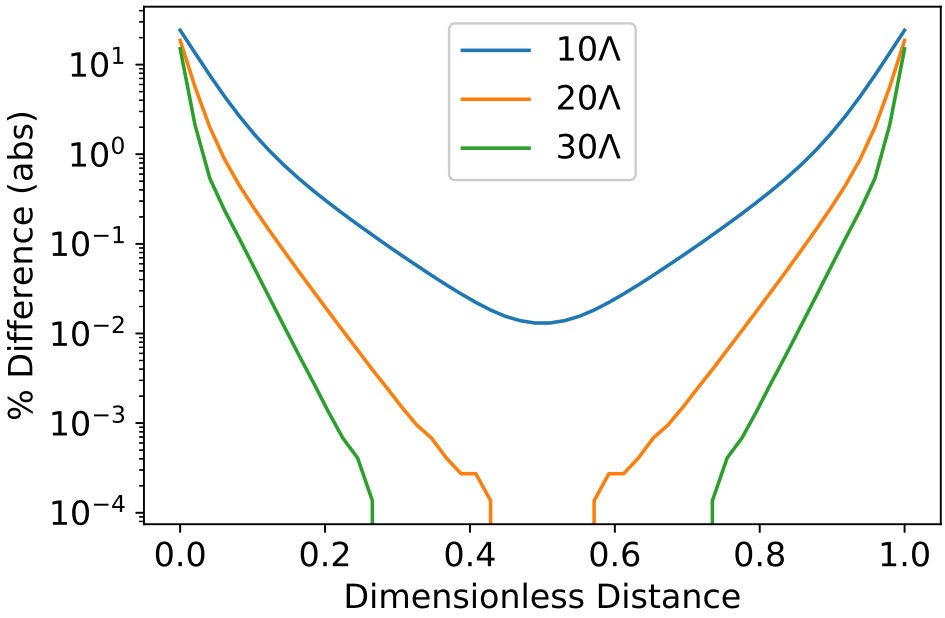

Figure 6: Deviation from kinetic theory, abs. % difference.

Additionally, we find that these simulations are sensitive to the heat flux calculation, and require many more iterations to converge the heat flux as the spectral radius grows closer to 1 as the simulation domain grows larger. This effect may be mitigated in the future research through a pseudo-scattering approach, however.

5. CONCLUSIONS

We present a method for predicting thermal conductivity using deterministic grey phonon transport in the SMRT approximation and the SAAF formulation with the advantages of having the flexibility to use arbitrarily higher-order finite elements, and structured or unstructured meshes with curved surfaces. These features offer computational flexibility for material interfaces which may contain curved features, or for automatic mesh refinement near material interfaces. Our method was verified using a MMS study and demonstrated that convergence rates do not suffer greatly by using meshes with curved surfaces, similar to previous work by Woods.

Our results also compare favorably with previous results of phonon transport temperature profiles in 1D thin silicon films, and previous deterministic transport simulations using identical approximations, and spatial and angular discretizations by Harter et al.

We demonstrate that in larger domain thicknesses, the effect of boundaries are mitigated which agrees with the transition from ballistic to diffuse phonon transport as noted by various previous work. However, as shown in previous work by Harter et al., boundary effects are also heavily influenced by the mesh coarseness and can be mitigated through mesh refinement near the boundaries.

6. FUTURE WORK

Previous work by Harter et al. has taken a slightly different approach when coupling the spectral effects of frequency dependent phonon transport by using a corrective term which changes based on the mismatch between the transport simulations and the expected equilibrium values [26].

Future research will examine temperature and frequency-dependent phonon transport through linearization of the Bose-Einstein phonon emission source in Eq. 9 and a corrective term which accounts for the disparity between the total phonon scattering term and the total phonon emission term. The linearization and iterative method together resembles a phonon capture and simultaneous re-emission, hence its designation as a pseudo-scattering iteration. Since the method also uses temperature dependent values, temperature must also be iterated upon.

Although the linearization approach is novel in phonon transport simulations, this methodology has previously been applied with success to thermal radiation transport. In future work the frequency, and temperature dependent SAAF-SMRT-PRT equation will be linearized, use angularly dependent mean free path data to solve for angular phonon intensities, and use those radiances to determine the thermal properties through discrete summations weighted by molecular dynamics simulations.

ACKNOWLEDGMENT

The authors acknowledge the financial support of Pacific Northwest National Laboratory (PNNL). PNNL is operated by Battelle Memorial Institute for the U.S. Department of Energy under Contract No. DE-AC05-76RL01830. This work was supported by the National Nuclear Security Administration, Tritium Sustainment Program through contract with Oregon State University and University of California-Riverside.

REFERENCES

1. A. Majumdar. Microscale Heat Conduction in Dielectric Thin Films. *Journal of Heat Transfer*, **115**, *7*, pp. 7-16 (1993).

2. B. Yilbas, and Y. Bin Mansoor. Phonon Transport in Two-Dimensional Silicon Thin Film: Influence of Film Width and Boundary Conditions on Temperature Distribution. *European Physical Journal B*, **85**, pp. 234-242 (2012).

3. J.R. Harter. Predicting Thermal Conductivity in Nuclear Fuels Using Rattlesnake-Based Deterministic Phonon Transport Simulations. Masters Thesis, Oregon State University (2015).

4. J. Charpin et al. Investigation of γ Lithium Aluminate as Tritium Breeding Material for a Fusion Reactor Blanket, *Fusion Engineering and Design*, **8**, pp. 407-413 (1989).

5. D. McMorrow. Tritium. Technical Report JSR-11-345, JASON - The MITRE Corporation (2011).

6. S. Sohinki. Tritium Readiness Campaign. National Nuclear Security Administration (2015).

7. U.S. Department of Energy. Tritium and Enriched Uranium Management Plan Through 2060, Report to Congress (2015).

8. D.J. Senor. Recommendations for Tritium Science and Technology Research and Development in Support of the Tritium Readiness Campaign, PNNL-22873 (2013).

9. S. Hu, A.M. Casella, C.A. Lavender, D.J. Senor, and D.E. Burkes. Assessment of Effective Thermal Conductivity in U–Mo Metallic Fuels. *Journal of Nuclear Materials*, **462**, (2015).

10. D. Anistratov. On Iteration Method for Steady-State Boltzmann Transport Problem. Personal Communication, (2019).

11. C. Kittel. *Introduction to Solid State Physics, 8th Ed.* John Wiley & Sons, Inc. (2005).

12. A.C Sparavigna. The Boltzmann Equation Of Phonon Thermal Transport Solved In the Relaxation Time Approximation – I – Theory. *Mechanics, Materials Science & Engineering Journal*, Magnolithe, **3**, pp. 34-45 (2016).

13. A. Mittal, and S. Mazumder. Monte Carlo Study of Phonon Heat Conduction in Silicon Thin Films Including Contributions of Optical Phonons. *Journal of Heat Transfer*, **132**, (2010).

14. J.M. Ziman. *Electrons and Phonons: The Theory of Transport Phenomena in Solids.* Oxford University Press, London, United Kingdom (1960).

15. V.M. Laboure, R.G. McClarren, and Y. Wang. Globally Conservative, Hybrid Self-Adjoint Angular Flux and Least-Squares Method Compatible with Voids. *Nucl. Sci. Eng.*, **185**, pp. 294-306 (2017).

16. J.E. Morel, and J.M. McGhee. A Self-Adjoint Angular Flux Equation. *Nucl. Sci. Eng.*, **132**, pp. 312 (1999).

17. MFEM: Modular Finite Elements Library, mfem.org.

18. J. Carrete et al. almaBTE: A Solver of the Space-Time Dependent Boltzmann Transport Equation for Phonons in Structured Materials. *Computer Physics Communications*, **220**, pp. 351-362 (2017).

19. D.N. Woods. High Order Finite Elements S_N Transport in X-Y Geometry on Meshes with Curved Surfaces in the Thick Diffusion Limit. Masters Thesis, Oregon State University.

20. D.N. Woods. Discrete Ordinates Radiation Transport using High-Order Finite Element Spatial Discretizations on Meshes with Curved Surfaces. Doctoral Dissertation, Oregon State University, (2018).

21. D.N. Woods, and T.S. Palmer. R-Z Geometry Discrete Ordinates Radiation Transport Using Higher-Order Finite Element Spatial Discretizations on Meshes with Curved Surfaces. *Journal of Computational and Theoretical Transport*, **48**, pp. 109-128 (2019).

22. Y. Wang, H. Zong, and R.C. Martineau. Diffusion Acceleration Schemes for Self-Adjoint Angular Flux Formulation with a Void Treatment. *Nucl. Sci. Eng.*, **176**, pp. 201-225 (2014).

23. M.L. Adams and E.W. Larsen. Fast Iterative Methods for Discrete-Ordinates Particle Transport Calculations. *Progress in Nuclear Energy*, **40**, pp. 3-159 (2002).

24. J.R. Harter, P.A. Greaney, and T.S. Palmer. Characterization of Thermal Conductivity using Deterministic Phonon Transport in Rattlesnake. *Trans. Am. Nucl. Soc.*, **112**, pp. 829-832 (2015).

25. J.R. Harter, L. de Sousa Oliveira, A. Truszkowska, T.S. Palmer, and P.A. Greaney. Deterministic Phonon Transport Predictions of Thermal Conductivity in Uranium Dioxide With Xenon Impurities. *Journal of Heat Transfer*, **140**, (2018).

26. J.R. Harter, S.A. Hosseini, T.S. Palmer, and P.A. Greaney. Prediction of Thermal Conductivity in Dielectrics Using Fast, Spectrally-Resolved Phonon Transport Simulations. *International Journal of Heat and Mass Transfer*, **144**, (2019).

CONSISTENT TEMPERATURE AND INTENSITY CALCULATIONS FROM DETERMINISTIC MULTI-FREQUENCY PHONON TRANSPORT

Nicholas H. Whitman[1*], Todd S. Palmer[1*], P. Alex Greaney[2], Dmitriy Y. Anistratov[3], Douglas E. Burkes[4], and David J. Senor[4]

[1]Oregon State University, School of Nuclear Science and Engineering
3451 SW Jefferson Way, Corvallis, OR 97333

[2]University of California - Riverside, Department of Mechanical Engineering
Bourns Hall A342, 900 University Avenue, Riverside, CA 92521

[3]North Carolina State University, Department of Nuclear Engineering
2500 Stinson Drive, Raleigh, NC 27607

[4]Pacific Northwest National Laboratory, Nuclear Fuels and Materials
902 Battelle Blvd, Richland, WA 99354

[*]Corresponding authors: whitmann@oregonstate.edu, palmerts@engr.orst.edu

ABSTRACT

In this work, we present an algorithm which solves a version of the energy-conserving, multi-frequency, and temperature-dependent Boltzmann transport equation which is solved by means of a linearization method. The multi-frequency and temperature-dependent phonon transport equation in self-adjoint angular flux form is spatially discretized using higher-order finite elements on unstructured meshes with curved surfaces. The angular domain is discretized using the discrete ordinates method with angular quadratures informed by spectral molecular dynamics simulations, containing 26 unique directions, each with 5 sub-groups of temperature dependent phonon mean free paths. In the full paper, we will show results from multi-frequency test problems expanding on previous work using a frequency-integrated (grey) phonon formulation.

KEYWORDS: frequency, temperature, phonon transport, self-adjoint angular flux, MFEM

1. INTRODUCTION

A priori thermal conductivity predictions are valuable for material scoping studies and in situations which the measurements are costly or prohibitive. These types of simulations are also extremely valuable for informing experiments, and assisting in the identification and answering of fundamental science questions.

We aim to demonstrate the solution of a frequency and temperature dependent radiative phonon transport equation in the Single-Mode Relaxation Time (SMRT) approximation to solve for thermal conductivity profiles in lithium aluminate. Lithium aluminate is a ceramic material of interest as a fusion breeder candidate.

This work expands on previous work which demonstrated deterministic solutions of the Self-Adjoint Angular Flux (SAAF) formulation of the grey SMRT phonon transport equation to obtain thermal conductivity profiles in lithium aluminate [1].

2. METHODS

Our approach to the non-linear coupling between the phonon intensity and the material temperature is motivated by a mature algorithm used in the thermal radiation transport community, which employs a Newton's iteration on the non-linear dependence of the Planck function on material temperature. In this application, the temperature and the phonon emission are constrained through the non-linear Bose-Einstein distribution.

We will derive the equation used in this work with the spatially first order transport equation and the process for the SAAF form is similar and self-consistent with this approach. We first start with the steady-state SMRT phonon radiative transport (PRT) equation driven by isothermal boundary conditions,

$$\boldsymbol{\Omega} \cdot \boldsymbol{\nabla} I(\boldsymbol{r}, \omega, \Omega, p) + \frac{I(\boldsymbol{r}, \omega, \Omega, p)}{\Lambda(\omega, p, T)} = \frac{I^0(\omega, p, T)}{\Lambda(\omega, p, T)}, \tag{1}$$

where $I^0(\omega, p, T)$ is the angular equilibrium phonon radiance, an angular phonon emission term based on temperature. We now linearize the equilibrium radiance on the right hand side by addition of a partial derivative around some temperature T^* known from previous iteration, and evaluate the mean-free-path $\Lambda(T^*)$ at that temperature to obtain

$$\boldsymbol{\Omega} \cdot \boldsymbol{\nabla} I(\boldsymbol{r}, \omega, \Omega, p) + \frac{I(\boldsymbol{r}, \omega, \Omega, p)}{\Lambda(\omega, p, T^*)} = \frac{1}{\Lambda(\omega, p, T^*)} \left[I^0(\omega, p, T^*) + \frac{\partial I^0}{\partial T}(\omega, p, T^*)(T - T^*) \right]. \tag{2}$$

We define the phonon emission term (PET) $\tilde{W}^0$ as

$$\tilde{W}^0(T) = \sum_p \int_0^{\omega_{max}} d\omega \frac{I^0(\omega, p, T)}{\Lambda(\omega, p, T)} \tag{3}$$

and phonon scattering term (PST) $\tilde{W}_s$ as

$$\tilde{W}_s(T) = \sum_p \int_0^{\omega_{max}} \int_{4\pi} \frac{d\boldsymbol{\Omega} d\omega}{4\pi} \frac{I(\boldsymbol{r}, \omega, \boldsymbol{\Omega}, p)}{\Lambda(\omega, p, T)} \tag{4}$$

and note that the implicit energy balance relationship gives rise to equality of the PET and PST. We also now linearize the PET around T^*

$$\tilde{W}^0(T^*) + (T - T^*) \frac{d\tilde{W}^0}{dT}|_{T=T^*} = \tilde{W}_s(T^*), \tag{5}$$

which yields an expression for the temperature increment based on the energy balance relationship

$$T - T^* = \left[\frac{d\tilde{W}^0}{dT}|_{T=T^*} \right]^{-1} (\tilde{W}_s(T^*) - \tilde{W}^0(T^*)). \tag{6}$$

Substituting the temperature increment in Eq. (6) into Eq. (2), and defining

$$\gamma(\omega, p, T^*) = \left[\frac{d\tilde{W}^0}{dT}|_{T=T^*}\right]^{-1} \frac{\partial I^0}{\partial T}|_{T=T^*}, \tag{7}$$

we obtain the linearized SRT-PRT with explicit pseudo-scattering

$$\boldsymbol{\Omega} \cdot \boldsymbol{\nabla} I + \frac{I}{\Lambda(T^*)} = \frac{1}{\Lambda(T^*)} \left(I^0(T^*) - \gamma(T^*)\tilde{W}^0(T^*)) \right) + \frac{\gamma(T^*)}{\Lambda(T^*)} \sum_p \int_0^{\omega_{max}} \int_{4\pi} \frac{d\boldsymbol{\Omega} d\omega}{4\pi} \frac{I(\boldsymbol{r}, \omega, \boldsymbol{\Omega}, p)}{\Lambda(\omega, p, T)} \tag{8}$$

Postponing a detailed discussion of the discretization methods for the full paper, our method utilizes the discrete ordinates (S_N) angular discretization, spatial discretization through higher-order finite elements in MFEM – a modular C++ finite element library, and an angle-frequency discretization developed to preserve behaviors observed through molecular dynamics research [2]. The angle-frequency approach allows computation of the PST though a discrete summation based on weighting terms, allowing for integration into existing S_N method used in the frequency-integrated approach.

To solve this equation, we iterate on temperature and the PST. The outer iteration is on temperature and the inner iteration converges the PST. The inner iterate loops through each discrete angle/mean-free-path group pre-computed by molecular dynamics, and computes a PST after the last group, and repeats this until the PST is converged within some predefined tolerance at a given fixed temperature T^*. The temperature is then updated through the temperature increment relationship, and the outer iteration continues again until the temperature converges within some predefined tolerance. The iteration scheme is presented in Algorithm 1.

At the end of the simulation, the heat flux is computed through another discrete summation which is recast from the frequency integrated form

$$\vec{q} = \sum_G \vec{\Omega}_g I_g w_g \longrightarrow \vec{q} = \sum_G \vec{\Omega}_g I_g [\Gamma_g(T^*) B_g(T^*)] \tag{9}$$

to a form weighted by temperature and frequency group which was pre-computed from molecular dynamics simulations. The thermal conductivity profile is created by using the heat flux and temperature gradient through either a continuous representation or a domain-averaged representation which is used in this work.

Eq. 8 is solved in each angle-frequency group and is driven by a fixed angular source dependent *only* on temperature, which is fixed for each inner iteration, and a transport calculated quantity which changes with each inner iteration.

3. CONCLUSIONS

We intend to present our findings on the performance of this multi-frequency, temperature-dependent phonon transport algorithm by expanding on previous work which examining a grey phonon formulation in the same framework and discretization.

Algorithm 1 An iterative algorithm for solving frequency and temperature dependent deterministic phonon transport equation in the SAAF form

while $||\Delta T^{(\ell)}(\vec{r})||_\infty > \epsilon_T$ **do**
  $\ell = \ell + 1$
  while $||\Delta \tilde{W}_s^{(k,\ell)}(\vec{r})||_\infty > \epsilon_s$ **do**
    $k = k + 1$
    for $\vec{\Omega}_g$ *in* $\vec{\Omega}$ **do**
      $-\vec{\Omega}_g \cdot \nabla \left[\Lambda_g[T^{(\ell)}]\vec{\Omega}_g \cdot \nabla I_g^{(k+1,\ell)}\right] + \frac{1}{\Lambda_g[T^{(\ell)}]} I_g^{(k+1,\ell)} =$
      $-\vec{\Omega}_g \cdot \nabla \left[I_g^0[T^{(\ell)}] - \gamma_g[T^{(\ell)}]\left(\tilde{W}^0[T^{(\ell)}] - \tilde{W}_s[T^{(\ell)}, I_g^{(k,\ell)}]\right)\right]$
      $+\frac{1}{\Lambda_g[T^{(\ell)}]}\left[I_g^0[T^{(\ell)}] - \gamma_g[T^{(\ell)}]\left(\tilde{W}^0[T^{(\ell)}] - \tilde{W}_s[T^{(\ell)}, I_g^{(k,\ell)}]\right)\right]$
    end
    $\tilde{W}_s^{(k+1,\ell)} = \sum_G A_g[T^{(\ell)}]B_g[T^{(\ell)}]I_g^{(k+1,\ell)}$
    $\Delta \tilde{W}_s^{(k+1,\ell)} = \tilde{W}_s^{(k+1,\ell)} - \tilde{W}_s^{(k,\ell)}$
  end
  $\tilde{W}_s^{(\ell+1)} = \tilde{W}_s^{(k+1,\ell)}$
  $I^{(\ell+1)} = I^{(k+1,\ell)}$
  $T^{(\ell+1)} = T^{(\ell)} + \left(\frac{\partial \tilde{W}^0}{\partial T}|_{T=T^{(\ell)}}\right)^{-1}(\tilde{W}_s^{(\ell+1)} - \tilde{W}^0)$
  $\Delta T^{(\ell+1)} = T^{(\ell+1)} - T^{(\ell)}$
end
$\hat{T} = T^{(\ell+1)}$
$\hat{I} = I^{(\ell+1)}$
$\vec{q} = \sum_G \vec{\Omega}_g \Gamma_g[\hat{T}]B_g[\hat{T}]\hat{I}_g$
$k_x = -\frac{1}{L}\int \frac{\vec{q}\cdot\hat{x}}{\nabla\hat{T}\cdot\hat{x}}\, dx$

ACKNOWLEDGEMENTS

The authors acknowledge the financial support of Pacific Northwest National Laboratory (PNNL). PNNL is operated by Battelle Memorial Institute for the U.S. Department of Energy under Contract No. DE-AC05-76RL01830. This work was supported by the National Nuclear Security Administration's Tritium Sustainment Program through contract with Oregon State University and University of California-Riverside.

REFERENCES

[1] N. H. Whitman et al., "Grey Phonon Transport Prediction of Thermal Conductivity in Lithium Aluminate with Higher-Order Finite Elements on Meshes with Curved Surfaces," *Proc. of ICTT-26*, Paris, France, September 22-27, 2019. (In Review).

[2] J.R. Harter, S.A. Hosseini, T.S. Palmer, and P.A. Greaney. "Prediction of Thermal Conductivity in Dielectrics Using Fast, Spectrally-Resolved Phonon Transport Simulations," *International Journal of Heat and Mass Transfer*, **144**, (2019).